



# Thermal and Mechanical Stability of Austenite in Metastable Austenitic Stainless Steel

A.A. TIAMIYU, SHITENG ZHAO, ZEZHOU LI, A.G. ODESHI, and J.A. SZPUNAR

The roles of grain size, texture, strain, and strain rate on the thermal and mechanical stability of austenite in AISI 321 metastable austenitic stainless steel were studied. Ultrafine grain (UFG), fine grain (FG), and coarse grain (CG) specimens with average grain sizes of 0.24, 3, and 37  $\mu\text{m}$  sizes, respectively, were investigated. To determine the thermal stability of austenite (TSA), samples were soaked in liquid nitrogen ( $-196^\circ\text{C}$ ) for varying times between 0.5 and 24 hours. On the other hand, the mechanical stability of austenite (MSA) was studied by subjecting cylindrical specimens to both quasi-static ( $4.4 \times 10^{-3} \text{ s}^{-1}$ ) and dynamic loading conditions (between 1300 and  $8800 \text{ s}^{-1}$ ). Thermally-induced  $\alpha'$ -martensite was only observed at an incubation time in AISI 321 to suggest an isothermal martensitic transformation occurred. Both Kurdjumov-Sachs ( $\{111\}_\gamma||\{110\}_\alpha$  and  $\langle\bar{1}01\rangle_\gamma||\langle\bar{1}\bar{1}1\rangle_\alpha$ ) and Nishiyama-Wasserman ( $\{111\}_\gamma||\{110\}_{\alpha'}$  and  $\langle112\rangle_\gamma||\langle011\rangle_{\alpha'}$ ) orientation relationships existed between the untransformed  $\gamma$  and thin-plate  $\alpha'$ -martensite. The thermally-induced phase transformation was highly suppressed in UFG specimens. While TSA decreased with an increase in grain size, MSA decreased with a decrease in grain size. While thin-plate  $\alpha'$  predominantly formed in the thermally-treated AISI 321 steel (FG and CG specimens only), lath and irregularly-shaped  $\alpha'$  formed in the specimens deformed under quasi-static and dynamic loading conditions, respectively. Irrespective of strain rate, deformation-induced  $\alpha'$  in UFG specimens inherited the morphology of the deformed austenite grain that is equiaxed. Irrespective of grain size, MSA also decreased with increase in strain (up to a critical strain for specimens deformed under dynamic loading condition) and decrease in strain rate. In the event of adiabatic shear band (ASB) formation in a specimen deformed at high strain rate, MSA increased as the ASB was approached due to the temperature rise in the ASB region. Electron backscattered diffractometry examination revealed that the evolution of both thermally- and deformation-induced martensite is orientation-dependent in FG and CG specimens. The instability (thermal and mechanical) of the austenite phase is highest in the RD/CD||[100]-oriented grains (RD and CD are rolling and compression directions, respectively), followed by grains oriented near RD/CD||[110] and RD/CD||[111], in that order. These findings could open a new window of engineering the initial texture of metastable austenitic stainless steel to either aid thermally and/or mechanically-stable austenite phase or promote both isothermal and deformation-induced martensitic phase transformation.

<https://doi.org/10.1007/s11661-019-05362-2>

© The Minerals, Metals & Materials Society and ASM International 2019

## I. INTRODUCTION

METASTABLE AUSTENITIC stainless steel (MASS) has a face-centered cubic (FCC) crystal structure and low stacking fault energy (SFE). It finds

application in energy (chemical and nuclear) and transportation sectors. MASS could be exposed to various degree of conditions that could result in the instability of its austenite phase in service, *i.e.*, martensitic phase transformation could occur. This could affect the properties of MASS, *e.g.*, loss of non-magnetic property of the MASS when  $\alpha'$ -martensite developed.<sup>[1]</sup> Some of these stability-deteriorating conditions include a cryogenic environment and exposure to an external load, either at low or high strain rates. In a cryogenic environment, the austenitic phase may become unstable, leading to the evolution of  $\alpha'$ -martensite. Generally, the martensitic transformation is displacive with definite crystallography,<sup>[2]</sup> and they are categorized into

A.A. TIAMIYU, A.G. ODESHI, and J.A. SZPUNAR are with the Department of Mechanical Engineering, University of Saskatchewan, Saskatoon, SK, Canada. Contact e-mail: ahmed.tiamiyu@usask.ca SHITENG ZHAO is with the University of California, Berkeley, Berkeley, CA. ZEZHOU LI is with the University of California, San Diego, La Jolla, CA 92093.

Manuscript submitted January 3, 2019.

athermal and isothermal transformations depending on the kinetics of transformation.<sup>[3–5]</sup> While the amount of martensites formed during athermal transformation depends solely on temperature, the amount of those that form during isothermal transformation is a function of both temperature and time.<sup>[6]</sup> For athermal transformation to occur and proceed, the thermal activation is not necessary.<sup>[7]</sup> In other words, only the thermodynamic driving force obtained by lowering temperature is adequate for athermal martensitic transformation. This thermodynamic driving force must overcome the elastic energy that opposes initiation at specific sites at and below the martensite start (Ms) temperature. Athermal martensitic transformation involves two steps. The first step is “barrier-less”, and it entails the evolution of martensite units, *i.e.*, martensite unit starts to form without the need to overcome any form of barrier. The second step is the growth of the martensite units which involves the migration of a glissile interface without thermal activation.<sup>[2]</sup> Meanwhile, the isothermal transformation has no definite Ms temperature, but it occurs with time (incubation) during isothermal holding. The amount of the product phase (martensite) in athermal transformation does not depend on time, but on temperature due to its intrinsic nature.<sup>[3]</sup> This is because no diffusion is involved in athermal transformation, and the composition of the product is the same as that of the parent (austenite) phase. While thermal activation implies statistical probability (*i.e.*, the same site will not always be the first to initiate the transformation process), the same site during a non-thermal activation process (athermal martensites) tends to repeatedly initiate the process of transformation. It, therefore, implies that the site with the lowest barrier is always the first one to initiate transformation during a non-thermal activation process.

Considering the thermal activation model for the transformation kinetics,<sup>[6]</sup> it has been predicted that when an athermal martensitic transformation is suppressed, an isothermal transformation will occur after some incubation time.<sup>[8]</sup> However, earlier work has reported the possible occurrence of both transformations (athermal and isothermal) in the same material.<sup>[9,10]</sup> On the kinetic, morphology and magnetic characteristics of thermally-induced martensite in Fe-30 pct Ni-3.6 pct Mo alloy, Yasar *et al.*<sup>[5]</sup> observed the occurrence of both athermal and isothermal martensitic transformation in the alloy using a scanning and transmission electron microscope. Using the temperature dependence of magnetic susceptibility measurement and X-ray diffraction techniques, Nam *et al.*<sup>[8]</sup> investigated the occurrence of martensitic transformation in micron-sized single and polycrystalline particles of an Fe-30.5 Ni (at. pct) alloy. They observed a reduction in Ms temperature from 215 K to 151 K when the grain size of the polycrystalline particles was reduced from 250 to 3.7  $\mu\text{m}$ , which translates to lowering the tendency for athermal martensitic transformation. Similarly, a 4.6  $\mu\text{m}$ -sized single crystal particle shows no Ms temperature, but instead, an isothermal martensitic transformation. On introducing grain boundaries and dislocation in the single crystal particle by sintering or

deformation, Ms temperature appeared and athermal martensite developed. This affirms the role of lattice defects on athermal martensitic transformation.

Under external load, where the stability of the austenite phase in MASS could be lost, deformation-induced martensitic transformation could also evolve at a critical strain.<sup>[11]</sup> The induced martensitic phase is reported to be stronger and harder than the austenite phase; resulting in a composite strengthening and a high strain hardening. It has been reported that  $\alpha$ -martensite acts as a reinforcing phase since it can withstand higher stress than austenite.<sup>[12]</sup> However, it is thought that the stability of the austenite phase will be different in MASS under quasi-static compression and those exposed to dynamic impact loading condition. This is because unlike the case under quasi-static loading (where temperature rise is negligible), a temperature rise occurs in a specimen subjected to dynamic impact load, which may influence the stability of the austenite phase. Martensitic phase transformation (*via* both cryogenic environment and exposure to external load) does not start simultaneously in all austenite grains in a MASS.<sup>[13]</sup> Therefore, the main objective of this work is to determine the role of crystallographic texture and grain size on the stability of austenite grains in AISI 321 austenitic stainless steel subjected to: (a) cryogenic environment and (b) a uniaxial compressive loading conditions at low (quasi-static) and high (dynamic) strain rates.

## II. MATERIALS AND METHODS

The AISI 321 steel used in this study is a metastable austenitic stainless steel that is stabilized with titanium (Ti) to reduce sensitization during high-temperature application. Samples of three different grain sizes, 0.24  $\mu\text{m}$  (ultrafine grain, UFG), 3  $\mu\text{m}$  (fine grain, FG), and 37  $\mu\text{m}$  (coarse grain, CG), were studied. The CG specimen was received in hot-rolled condition with a nominal composition (in weight percent) of 17.61 Cr, 9.17 Ni, 1.56 Mn, 0.42 Mo, 0.40 Si, 0.36 Ti, 0.30 Cu, 0.15 Co, and 0.044 C. The process of developing FG and UFG structures from the CG as-received sample is schematically shown in Figures 1(a) through (d). The CG (as-received) sample was first cryo-rolled up to 50 pct thickness reduction. While some of the cryo-rolled specimens were annealed at 750 °C for 10 minutes to develop UFG structure, others were annealed at 800 °C for 360 minutes to develop FG structure. More details on the thermo-mechanical process for developing UFG structure in the AISI 321 steel are provided in Reference 14. Investigation of thermal stability of austenite (TSA) involves soaking the steel samples in liquid nitrogen for varying times up to 24 hours (Figure 1(e)). To determine the mechanical stability of austenite (MSA), 4 mm × 4 mm cylindrical test specimens of UFG, FG and CG were machined with the axis of the specimen parallel to the rolling direction (RD) of the plate. Specimens were compressed under quasi-static and dynamic loading conditions (Figure 1(f)). Compression direction is parallel to RD. Quasi-static compression test was conducted using Instron R5500 mechanical

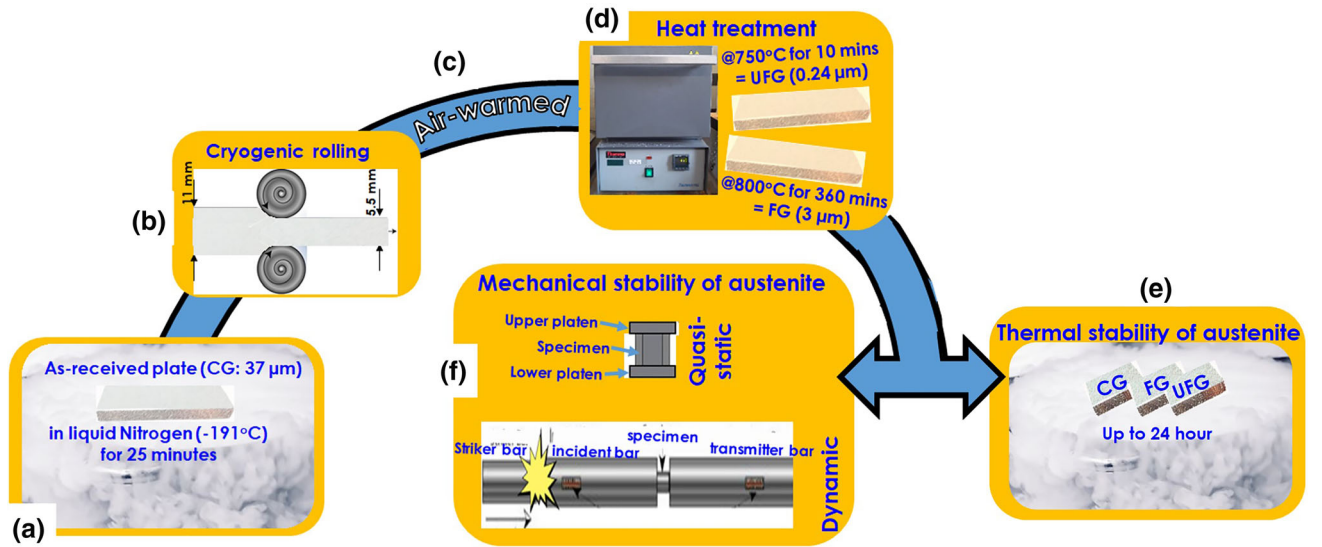


Fig. 1—Schematic drawing of the methodology: (a) through (d) development of UFG and FG structures, (e) samples in liquid nitrogen to investigate TSA and (f) compressed specimens under both quasi-static and dynamic shock loading to investigate MSA.

testing system with a 150 kN load cell at a true strain rate of  $4.4 \times 10^{-3} \text{ s}^{-1}$ . High strain rate test was conducted using the split Hopkinson pressure bar (SHPB) system at true strain rates between 1300 and  $8800 \text{ s}^{-1}$ . The working principles of SHPB system and the stress waves equations used in generating stress, strain, and strain rate data can be found in Reference 15. Hardness measurement was conducted using Mitutoyo Micro Vickers hardness testing machine (MVK-H1). The specimens were subjected to a load of 9.8 N for 10 seconds. The test was repeated four more times, and average values are reported for each specimen. All compression and hardness tests were conducted at room temperature.

Bruker D8 Discover diffractometer with Cr K $\alpha$  radiation was used to carry out X-ray bulk/macrotecture and phase identification measurements. Texture measurement was analyzed using Resmat software. Feritscope MP30E was also used to obtain the volume fraction of  $\alpha'$ -martensite. The actual martensite content is the feritscope reading times the correction factor of 1.7.<sup>[16]</sup> Metallographic preparation of specimens for microstructural analysis involved electrolytic polishing using a solution consisting of 35 pct sulfuric acid, 45 pct orthophosphoric acid and 20 pct de-ionized water as the electrolyte.

Electron backscattered diffractometry (EBSD) measurements were carried out using an SU 6600 Hitachi field emission scanning electron microscope coupled with an Oxford Instruments Nordlys Nano EBSD detector. AZTEC 2.0 data acquisition software was used to acquire the electron diffraction patterns with a binning of  $4 \times 4$  pixels and step size of 10 to 400 nm. Raw data were post-processed using the Oxford Instrument's Channel 5 post processing software. Transmission electron microscopy (TEM) and scanning transmission electron microscopy (STEM) analyses were performed using a FEI-Talos F200X microscope that is

coupled with a Super-X<sup>TM</sup> EDS detector at an operating voltage of 200 kV. Electron transparent disks for TEM analysis were prepared using a Struers TenuPol-3 twin-jet electro-polisher. The electrolyte containing a mixture of 90 pct methanol and 10 pct perchloric acid (vol pct) was used at  $-30^\circ\text{C}$  and at a voltage of 20 V. Meanwhile, focused ion beam (FIB) was used to accurately prepare TEM samples in the adiabatic shear band region formed in impacted specimens. All measurements and microstructural analysis were conducted on the ND-TD plane (for thermally-treated samples) and compression plane (for compressed specimens).

### III. RESULTS AND DISCUSSION

#### A. Initial Microstructure

Figure 2 shows the TEM micrographs of the UFG (Figure 2(a)), FG (Figure 2(b)), and CG (Figures 2(c) to (f)) specimens without thermal or mechanical treatments. While the near-absence of annealing twins was observed in the UFG specimen, their (twins) presence was confirmed in the FG and CG specimens. Stacking faults (Figure 2(d)) and near-absence of misfit around a particle that is confirmed to be TiC (Figures 2(e) and (f)) are also present in CG specimen. This could, therefore, imply that  $0.24 \mu\text{m}$  is near the critical grain size below which annealing twin cannot develop in AISI 321 stainless steel. A similar observation of twin suppression was observed in AISI 304 stainless steel (whose derivative is AISI 321) with a grain size of  $\sim 0.27 \mu\text{m}$ , developed by accumulative rolling that is followed by annealing at  $550^\circ\text{C}$  for 150 seconds.<sup>[17]</sup> Figure 3 shows the bulk texture result of the starting microstructure for the three grain sizes. UFG is significantly textured with Cube orientation. Strong R-Cube and Cu orientations with spread around  $\{112\}\langle012\rangle$ ,  $\{332\}\langle123\rangle$  and  $\{123\}\langle013\rangle$  orientations are observed in FG specimens;

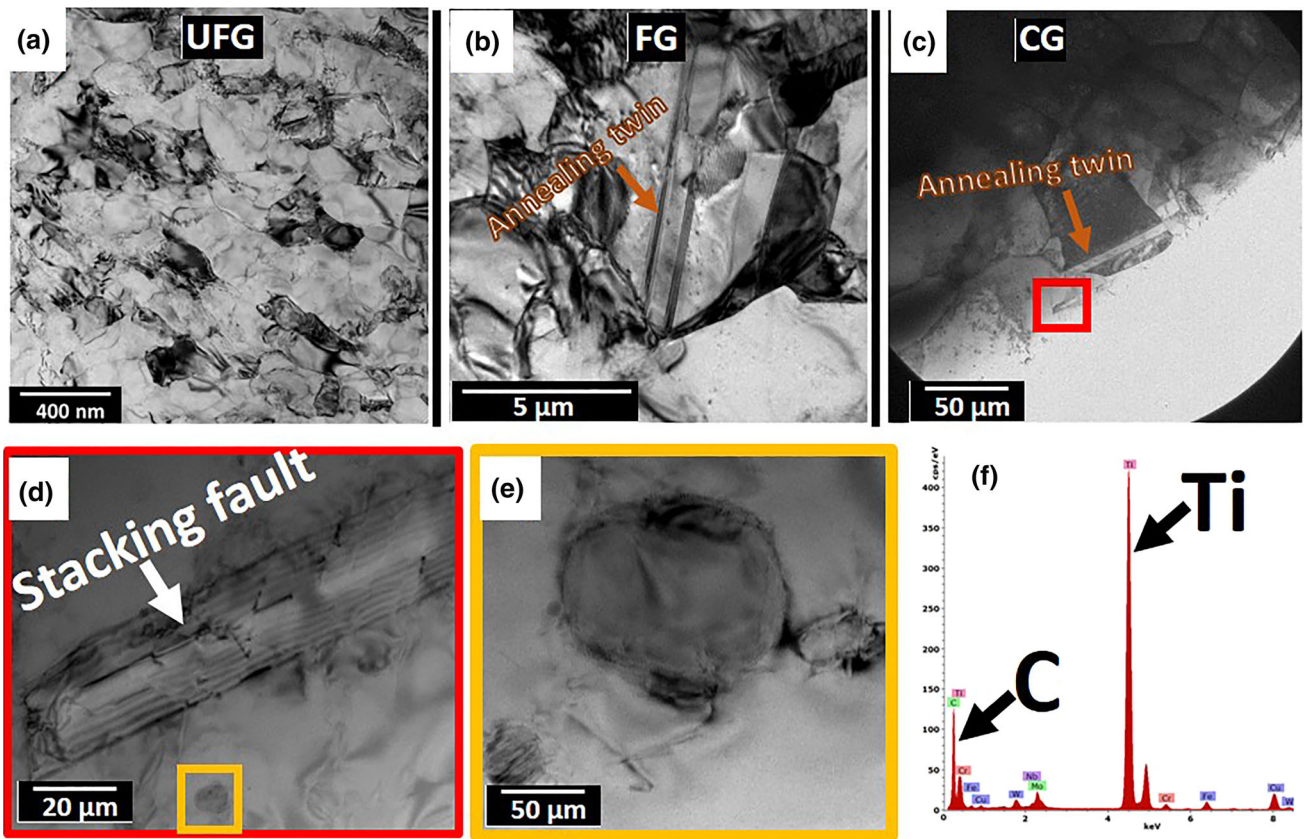


Fig. 2—TEM bright field micrographs of undeformed (a) UFG, (b) FG, and (c) through (e) CG samples. (f) is the EDS spectra of the TiC particle in (e).

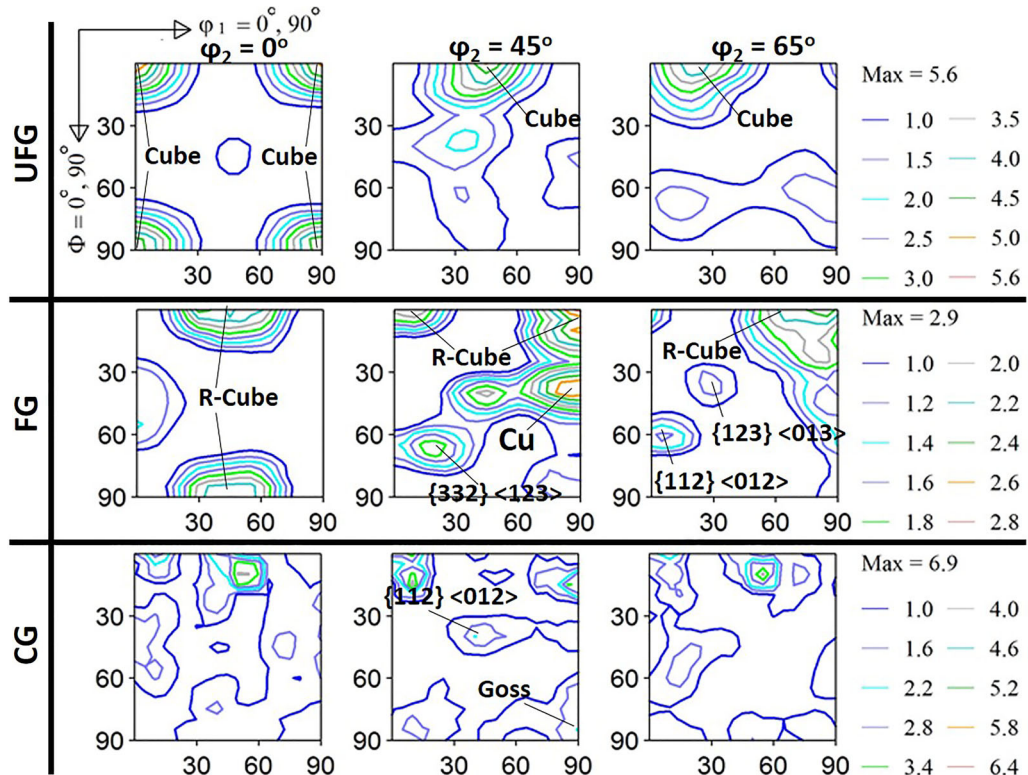


Fig. 3—Selected ODF  $\phi_2$  sections from the XRD measurement of the undeformed UFG, FG, and CG samples.

the intensities of which decreases as the grain size increases to CG structure.

### 1. Thermal stability of austenite (TSA)

Until now, the TSA in AISI 321 MASS has not been clearly clarified. It is certain that the  $\gamma$  phase becomes unstable in a cryogenic environment, thereby promoting the occurrence of martensitic phase transformation. However, it is not clear if phase transformation occurs athermally or isothermally, and by extension, how the role of grain size and crystallographic texture influences the evolution pattern.

The CG specimen was used to determine if martensitic phase transformation occurs athermally or isothermally by immersion in liquid nitrogen for different length of times until traces of  $\alpha'$ -martensite was observed. Figure 4 shows the EBSD maps of the specimen in the same area, before (Figures 4(a) through (c)) and after (Figures 4(d) through (f)) thermal treatments. After 20 minutes of immersion, there was no evidence of phase transformation as observed in Figure 4(d). Traces of phase transformation was however observed after additional 1 hour immersion (Figure 4(e)) in liquid nitrogen and the area fraction of the  $\alpha'$ -martensite trace increases with time (Figure 4(f)). The Kernel average misorientation (KAM) maps in Figure 4 also confirm the occurrence of cryogenic-induced defects that accompanied phase transformation. These defects increases (higher KAM values) with an increase in the exposure time in a cryogenic environment. The annealing twin planes in Figures 4(e) and (f) also show to be the least susceptible to martensitic phase transformation. Due to the observed kinetics, *i.e.*, the onset of phase

transformation after 1 hour (a cumulative of 120 minutes) or suppression of transformation at and below 20 minutes, it is concluded that phase transformation in AISI 321 stainless steel occurs isothermally in cryogenic condition. Athermal martensitic transformation is ruled out because no martensite was observed in AISI 321 stainless steel until an incubant time is reached despite being subjected to a cryogenic environment at  $-196^{\circ}\text{C}$ . This temperature is below the  $M_s$  temperature of the steel,  $-152.5^{\circ}\text{C}$ , estimated using Eq. [1].<sup>[18]</sup> The amount of athermal martensite that form depends on the degree of undercooling below  $M_s$  temperature and their character is a consequence of very rapid nucleation and growth such that the time taken (order of  $10^{-7}$  seconds) can be ignored.<sup>[19]</sup> The sketch that represents the kinetics of athermal and isothermal martensite transformations are presented in Figures 4(g) and (h), respectively. It is clear that the evolution of  $\alpha'$  is formed isothermally, having required an incubant time as shown in Figure 4(h).

$$M_s(^{\circ}\text{C}) = 1302 - 42(\text{Pct Cr}) - 61(\text{Pct Ni}) - 33(\text{Pct Mn}) - 28(\text{Pct Si}) - 1667(\text{Pct C} + \text{Pct N}) \quad [1]$$

Having observed that appreciable fraction of thermally-induced  $\alpha'$  could form in AISI 321 steel after 12 hours in liquid nitrogen (Figure 4), a new set of samples (UFG, FG, and CG specimens) were held in liquid nitrogen for 24 hours to evaluate the role of grain size on isothermal martensitic transformation. EBSD (Figures 5, 6, 8 and 9) and SEM (Figure 7) analyses were conducted on a selected area, before and after

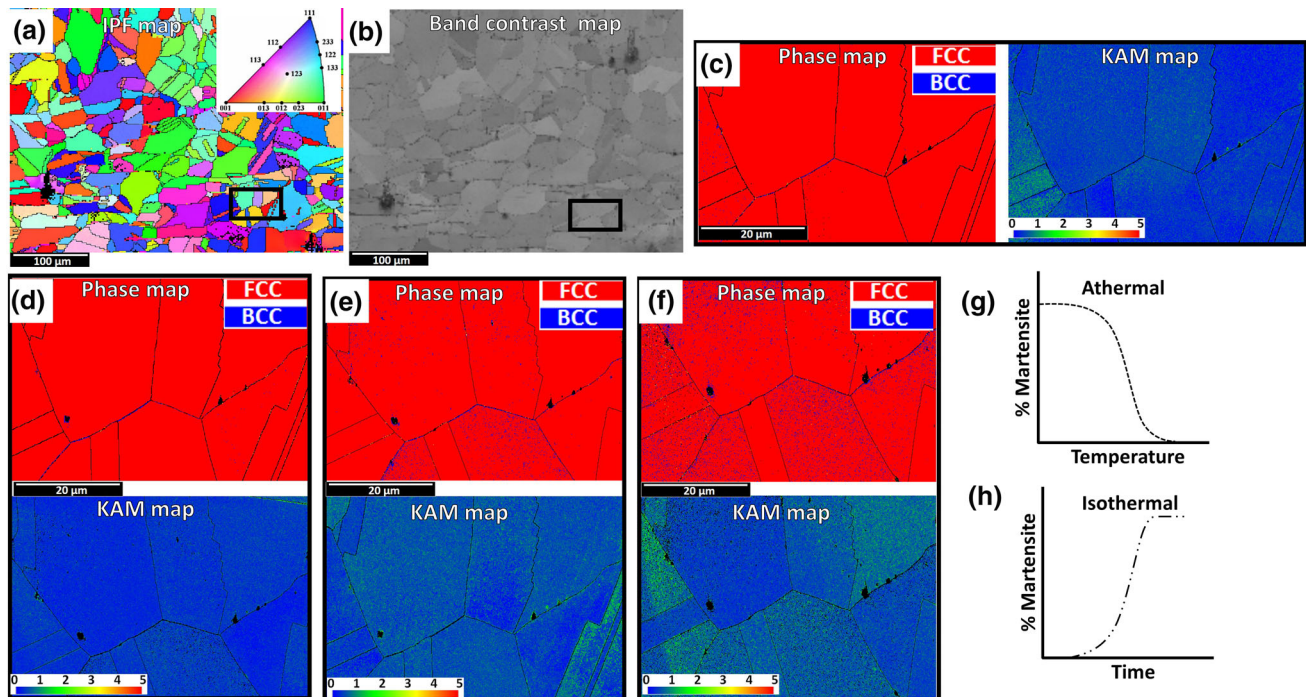


Fig. 4—EBSD maps (a) through (c) before thermal treatment and (d) through (f) successive increment of time in liquid nitrogen: (d) 20 min, (e) 1 h 20 mins, and (f) 13 h 20 mins. Sketch of kinetics of (g) athermal and (h) isothermal martensite formation.

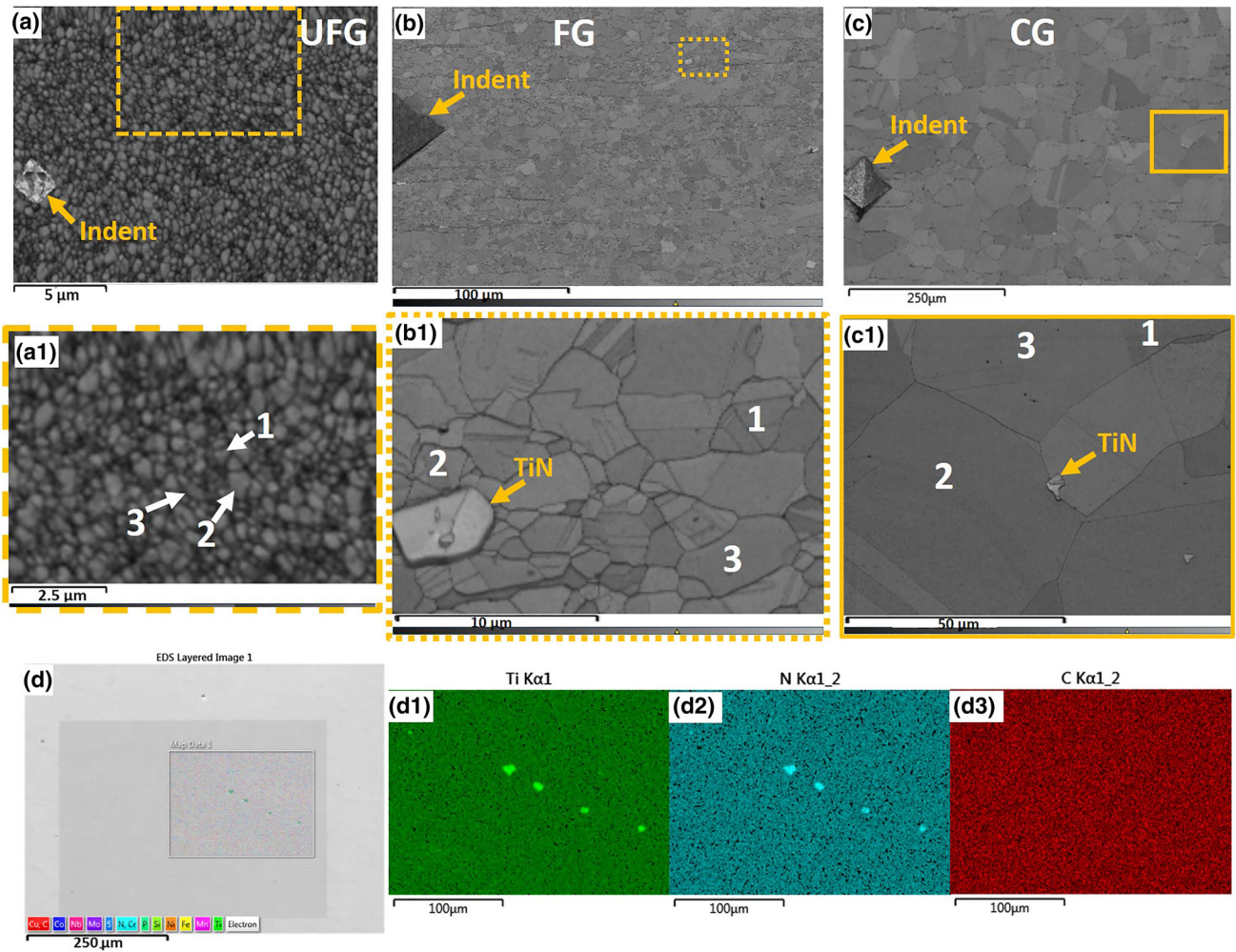


Fig. 5—Before thermal treatment: EBSD band contrast maps of (a) UFG, (b) FG, and (c) CG specimens. (a1), (b1) and (c1) are the corresponding high magnification of scanned area. (d) is the EDS maps confirming the presence of TiN particles ((d1), (d2) and (d3) are the corresponding EDS color maps for Ti, N and C, respectively).

thermal treatment, for each of the specimens with varying grain sizes. The EBSD band contrast maps of the selected area in UFG, FG and CG specimens before thermal treatment are presented in Figures 5(a) through (c), respectively. Figure 5(d) shows the EDS maps that confirm the presence of TiN particles in AISI 321 steel. In order to determine the role of grain orientations on phase transformation, the inverse pole figure (IPF) maps of grains with crystallographic orientations near  $RD||[111]$ , [110] and [100] were selected from Figure 5 and presented in Figure 6. The phase, band contrast (BC) and twin and KAM maps of the untreated selected grains are also presented. From Figure 6, it can be deduced that annealing twins are only present in FG and CG specimens irrespective of the grain orientation.

The SEM micrographs showing the regions before and after 24 hours of thermal treatment are presented in Figure 7. The figures show the evolution of plate-like martensite only occur in FG (Figures 7(e) and (h)) and CG (Figures 7(f) and (i)) as indicated by some arrows.

The absence of  $\alpha'$  plates in UFG specimen is possibly due to spatial restriction effect that resists the formation of isothermal martensite. This will subsequently restrict multi-variant transformation required to accommodate anisotropic transformation strain that occurred due to volume expansion. It can be concluded from these results that the area fraction of the thermally-induced  $\alpha'$  increases with increasing grain size. This result establishes that grain refinement to UFG structure increased the thermal stability of the austenite phase in AISI 321 stainless steel. In a different study, Matsuoka *et al.*<sup>[20]</sup> studied the thermal stability of Fe-16 pct Cr-10 pct Ni metastable stainless steel with grain sizes in the range of 1 to 80  $\mu\text{m}$ . They observed that the TSA increased with decrease in grain size. Notably, the FG and CG specimens formed fine and coarse  $\alpha'$  plates, respectively. This affirms the role of grain size on the size of thermally-induced  $\alpha'$ . The limitation of  $\alpha'$  plate by the prior  $\gamma$  grain size has been reported in another previous study.<sup>[21]</sup>

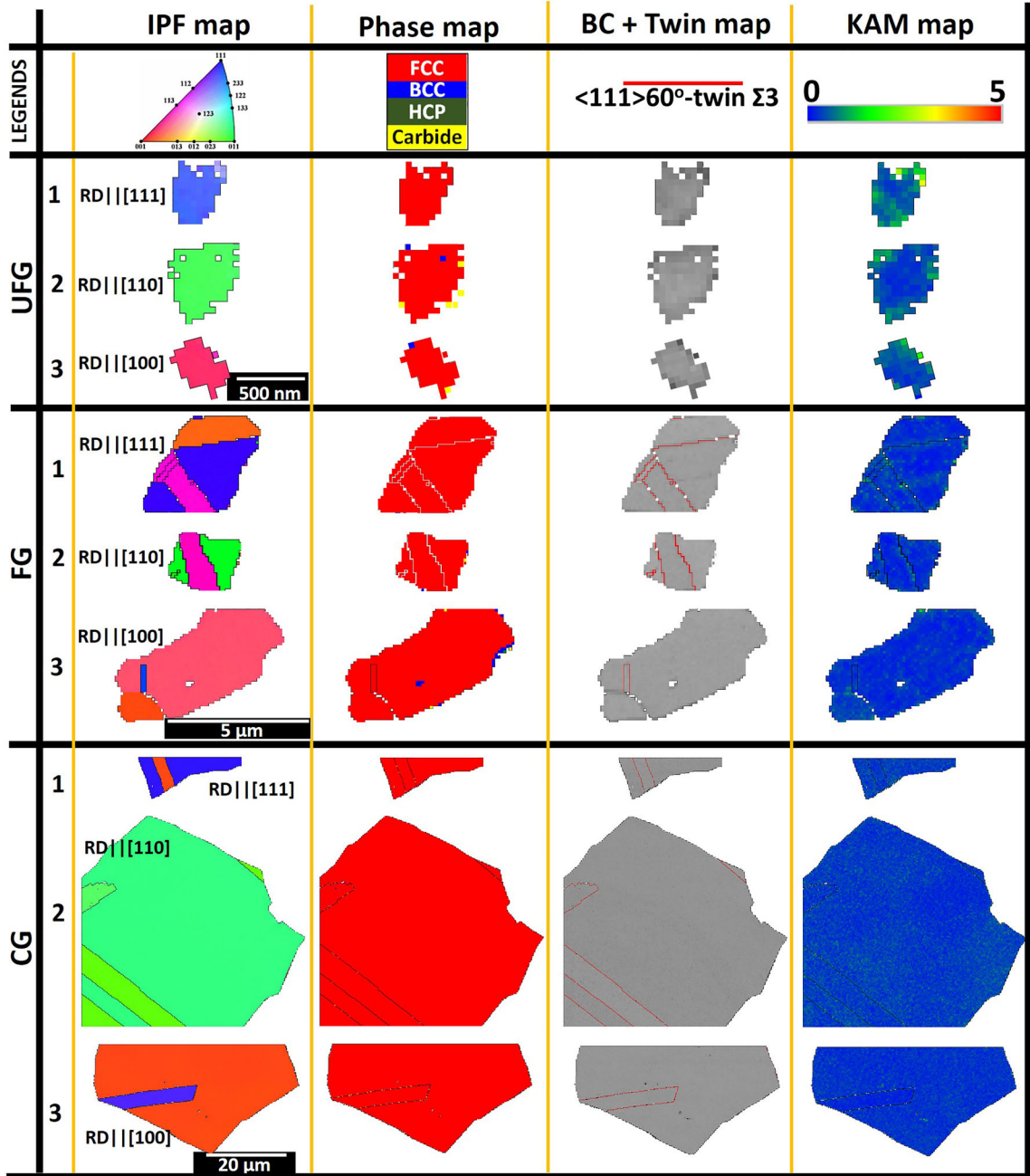


Fig. 6—Before thermal treatment: EBSD IPF, phase, BC/twin and KAM maps of selected grains in Figs. 5(a1) through (c1). Grains 1, 2, and 3 are RD||[111], RD||[110] and RD||[100]-oriented grains, respectively.

## 2. Role of crystallographic texture and annealing twins on thermal stability of austenite (TSA)

Although Figure 7 confirms that there is a critical grain size below which the nucleation of  $\alpha'$  plates becomes difficult (as in the case of UFG specimen), the uneven distribution of the nucleated  $\alpha'$  plates on the analyzed plane in FG and CG specimens hint that the nucleation of  $\alpha'$  is texture-dependent. The EBSD maps of the selected grains in Figure 6 after thermal treatment are now presented in Figure 8 to justify the texture-dependent of the phase transformation. Figure 8 shows no

phase transformation in the pre-selected grains from the earlier scanned area of FG specimen.

However, EBSD measurement on another location confirms phase transformation in near RD||[100] oriented grain (Figures 9(a) through (d)). Although  $\alpha'$  nucleated in all (RD||[111], [110] and [100]) crystallographic-oriented grains for CG specimens, it is clear from the phase maps in Figure 8 that RD||[100] grain is the least thermally-stable  $\gamma$  grain, followed by RD||[110] and [111] grains in that order. The EBSD IPF (Figures 9(e) and (g)) and phase maps (Figures 9(f) and (h))

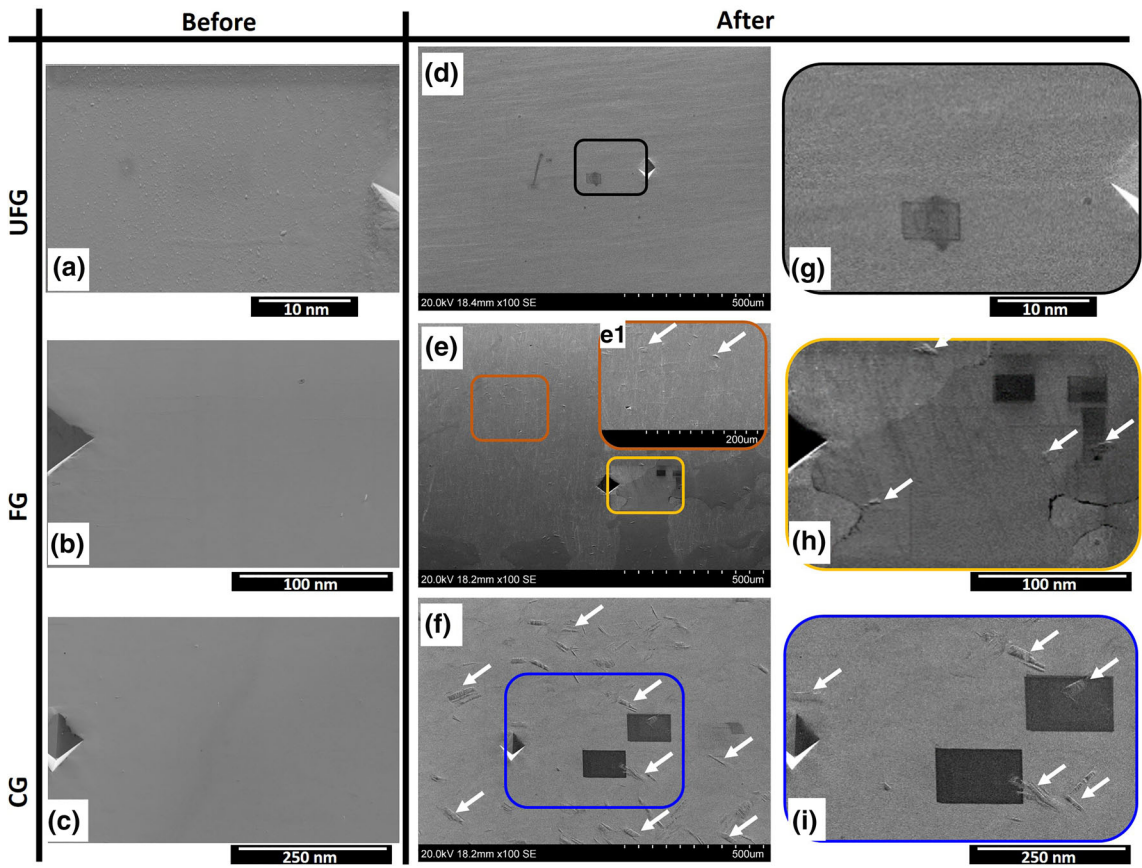


Fig. 7—SEM micrographs of the same region (a) through (c) before and (d) through (i) after thermal treatment. White arrows indicating some regions of thermally-induced martensite.

of another location in CG specimen show nucleation of  $\alpha'$  in austenite grains oriented near  $RD \parallel [100]$ , which is in agreement with the earlier observation. In all scanned regions (including FG and CG specimens), a higher fraction of  $\alpha'$  nucleated in  $RD \parallel [100]$  oriented grains as indicated by white contours in the standard stereographic IPF triangle in Figure 9(i). These findings could open a new window of engineering the initial texture of metastable austenitic stainless steel to either aid thermally and/or mechanically-stable austenite phase (by developing [111]-oriented grains) or promote both isothermal and deformation-induced martensitic phase transformation (by developing [100]-oriented grains).

The BC and twin maps of CG specimen in Figure 8 also confirmed the preferential nucleation of thermally-induced  $\alpha'$  at the annealing twin boundaries; an important nucleation site. The near-absence of annealing twins in austenite phase of UFG specimen could, therefore, also justify its (UFG specimen) high resistance to isothermal martensitic phase transformation. Notably, the nucleated  $\alpha'$  are bounded by transformation twins. The comparison of the KAM maps in Figures 6 and 8 shows an increase in the KAM value of the  $\gamma$  phase after thermal treatment. The KAM is a measure of local misorientation that indicates the strain distribution or stored elastic energy in the specimen. It is the average misorientation between each measured point and its neighbors which holds as long as the

misorientation do not exceed 5 deg.<sup>[22]</sup> The higher the KAM value, the higher the stored energy and strain in the specimen. Therefore, thermally-induced strain occurred during thermal treatment due to higher KAM value in Figure 8 than in Figure 6. Specifically, high KAM values are recorded at the  $\gamma\text{-}\alpha'$  and  $\alpha'\text{-}\alpha'$  boundaries in Figure 8. The misorientation gradient could imply the occurrence of plastic deformation in the  $\gamma$  phase to accommodate the shape change (or shape strain) of  $\alpha'$  during phase transformation.<sup>[21]</sup> Besides annealing twin boundaries, other authors have reported that carbide particles are potent nucleation site for thermally-induced  $\alpha'$  due to the misorientation that exists in the austenite phase at the particles' vicinity.<sup>[19,21]</sup> However, neither TiC nor TiN particles in AISI 321 stainless steel are found to be potential  $\alpha'$  nucleation sites. This is because there was no  $\alpha'$  observed to nucleate around the particles (white arrows in Figure 9(j)), and the misorientation gradient in the austenite phase at the particles' vicinity is nearly absent (Figure 9(k)).

### 3. Morphology and structure of thermally-induced $\alpha'$

There are primarily three different morphologies of martensite, namely, lath, thin plate, and lenticular. The evolution of these morphologies depends on the composition and the Ms temperature of the alloy.<sup>[23]</sup> Other factors (which can be related) such as the strength of

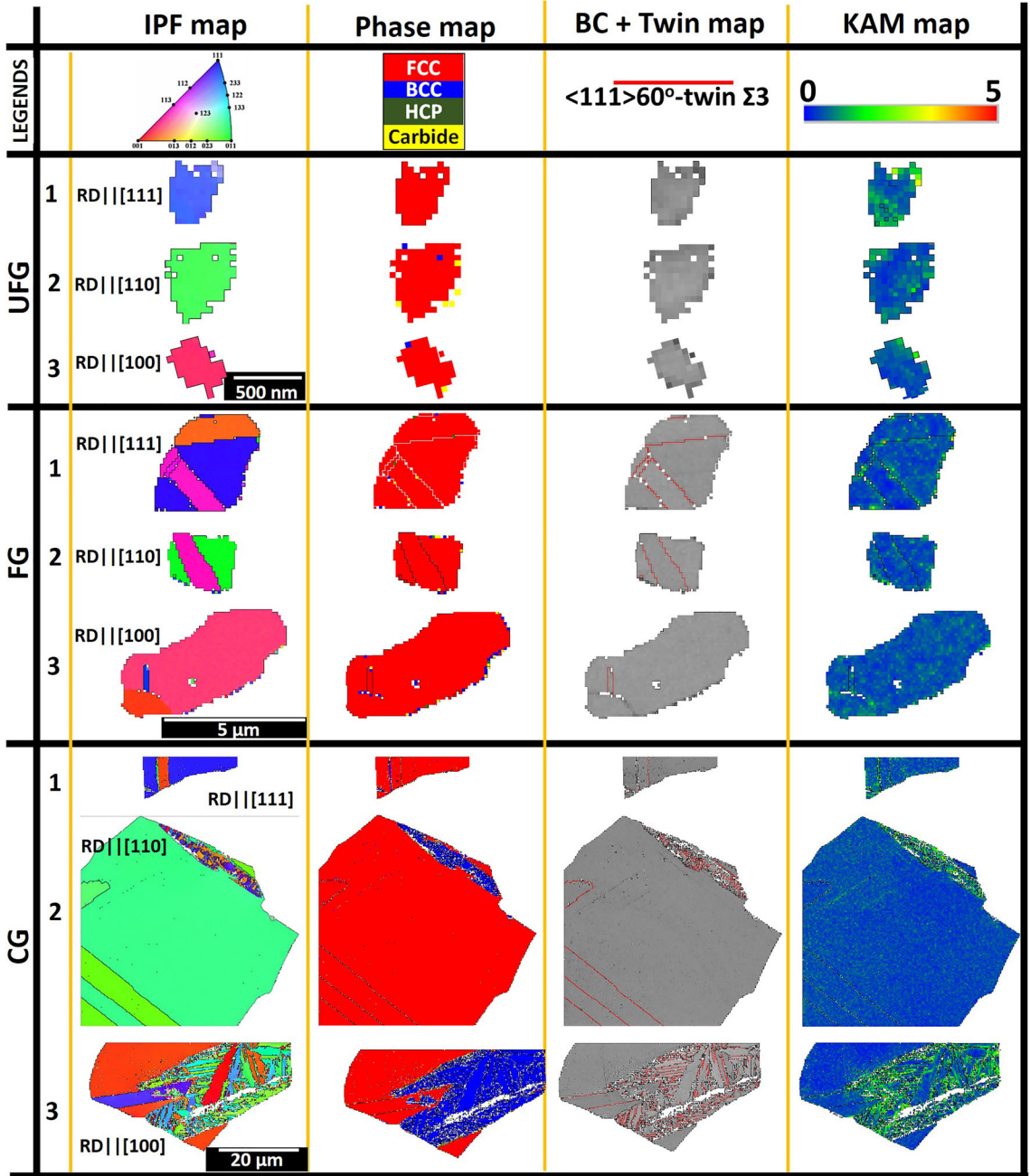


Fig. 8—After thermal treatment: EBSD IPF, phase, BC/twin, and KAM maps of selected grains in Figs. 5(a1) through (c1). Grains 1, 2, and 3 are RD||[111], RD||[110] and RD||[100]-oriented grains, respectively.

parent ( $\gamma$ ) and product ( $\alpha'$ ) phases, critical resolved shear stress for slip and twinning in  $\alpha'$  and SFE of  $\gamma$  have also been reported.<sup>[24,25]</sup> While lath  $\alpha'$  forms in the highest temperature regime (especially in the low carbon steels and Fe-Ni alloys), thin-plate  $\alpha'$  forms in the lowest temperature range in high alloyed steels.<sup>[26]</sup> The lenticular  $\alpha'$  however forms at an intermediate temperature regime between those of lath and thin-plate  $\alpha'$ . The formation range of  $\alpha'$  as a function of Ms temperature and carbon concentration in Fe-Ni-C alloy systems is schematically shown in Figure 10(a).<sup>[24]</sup> Although, AISI 321 stainless steel is a Fe-Cr-Ni alloy system with 0.044

C wt pct, Figure 10(a) can still provide useful information on the plausible  $\alpha'$  morphology with minimal deviation. Similarly, while lath  $\alpha'$  is characterized by high dislocation density due to strain accommodation induced by phase transformation, thin-plate  $\alpha'$  is characterized by a set of uniformly spaced transformation twins crossing throughout the plate.<sup>[21,23]</sup> Lenticular  $\alpha'$  has a lens-like morphology that contains three regions: the midrib (a region of highly dense and regularly spaced transformation twins), extended twinned region that emanates from the midrib and untwinned region (characterized by screw dislocations and a high density

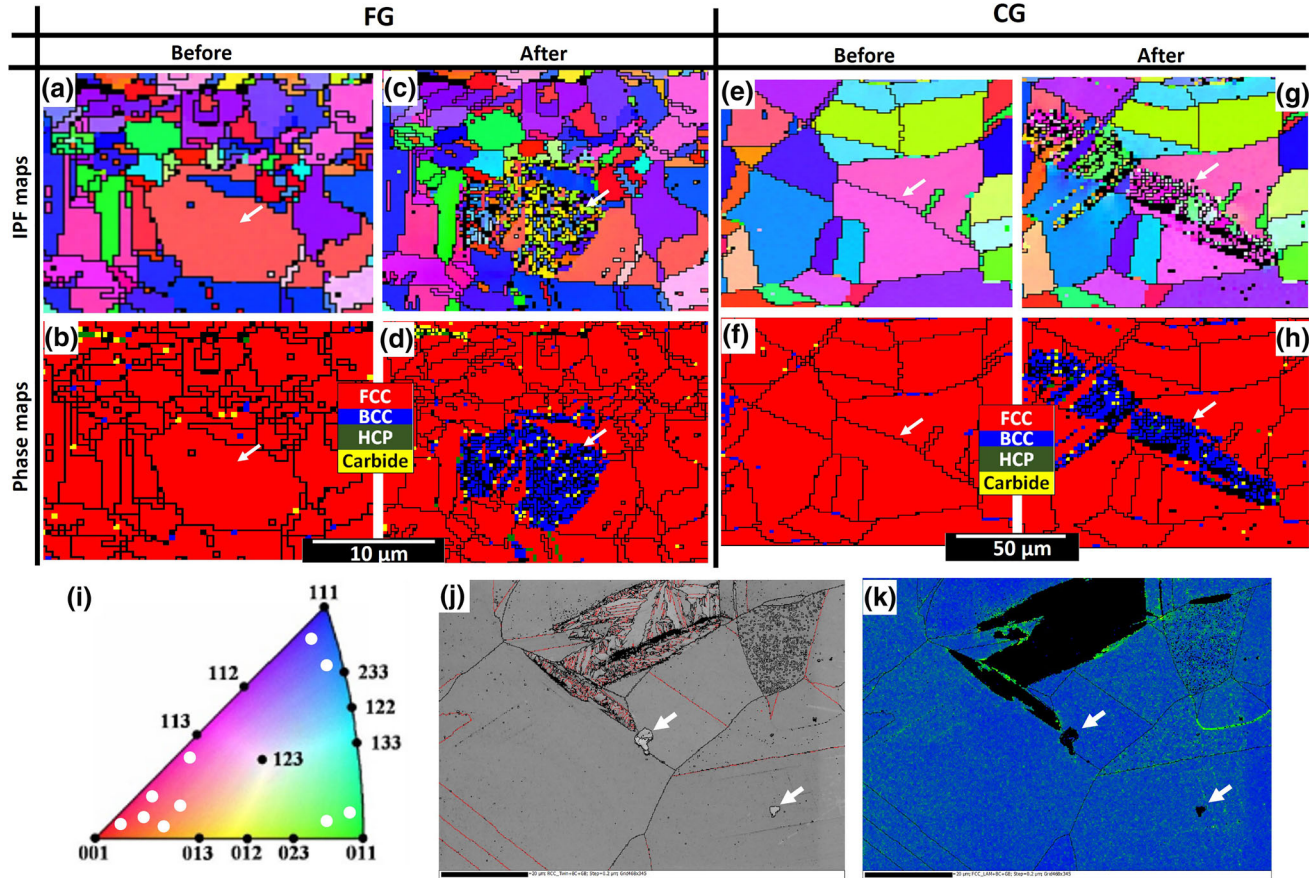


Fig. 9—Other regions in (a) through (d) FG and (e) through (h) CG specimens showing IPF and phase maps before and after thermal treatment; (i) contours in the standard stereographic IPF triangle showing the crystal orientation of austenite grains that developed martensite; (j) band contrast/twin and (k) KAM maps showing arrowed TiN particle site.

of tangled dislocations). It has been reported that the midrib of a lenticular  $\alpha'$  is a thin-plate  $\alpha'$  since both (midrib and thin-plate  $\alpha'$ ) have similar morphology, substructure, and crystallographic features.<sup>[24]</sup> Hence, the major difference between lenticular and thin-plate  $\alpha'$  is only in their growth behaviors; *i.e.*, during growth, thin-plate  $\alpha'$  retains its deformation mode of twinning and midrib exhibits a combination of twinning and slip modes.<sup>[19,21,24,26]</sup> Shibata *et al.*<sup>[26]</sup> reported that midribs in lenticular  $\alpha'$  could also be branched and kinked.

The higher magnification IPF and BC/twin maps for RD|[100] oriented coarse  $\gamma$  grain are presented in Figures 10(b) and (c), respectively. The thermally-induced martensite grains are mainly oriented near [110] and characterized by pronounced transformation twins. This observation suggests the induced  $\alpha'$  possess a thin-plate morphology. This is supported by tracing the AISI 321 carbon content and the thermal treatment temperature in Figure 10(a), although little deviation may exist. Relatively high austenite strength, low Ms temperature (as observed in Figure 10(a)), high tetragonality of  $\alpha'$  (*i.e.*, small twin shear, low magnitude of shape strain and low twin boundary energy) are reported to favor the formation of thin-plate  $\alpha'$ .<sup>[27]</sup> Considering the different direction in which the  $\alpha'$  grains are morphologically arranged, five possible growth

directions are indicated in Figure 10(b). Martensite grains in 1, 2, 3, and 4 directions confirmed grain boundaries serve as a viable nucleation site. The nucleation of grains labeled directions '3' and '4', from the grain boundaries are supported by considering Figure 5(c). There is the possible occurrence of 'burst' martensitic transformation phenomenon in which a martensite grain (such as the long [100] oriented  $\alpha'$  grain indicates as direction '3' in Figure 10(b)) nucleates a sequence of other plates (such as all the [110] oriented grain along direction '5'). These occur as a result of stress concentrations set up when the first plate reaches an obstruction such as grain boundary or another  $\alpha'$  plate such as grains aligned in direction '1'.<sup>[19,21]</sup> That is, the 'bursting' of grains aligned in direction '5' could be due to the stress concentration set up during growth as a result of the collision of grain labeled direction '3' on already isothermally nucleated grains in direction '1'. Figures 10(b) and (c) also show that the growth of some 'busted' martensites (grains in direction '5') are effectively hindered by the incoherent boundary of an existing annealing twin. Although incoherent twin boundaries could be likely sites for  $\alpha'$  nucleation,<sup>[19]</sup> it is confirmed that they can also actively hinder a growing  $\alpha'$ . By qualitative kinetic classification, the bursting phenomenon and isothermal martensitic transformation

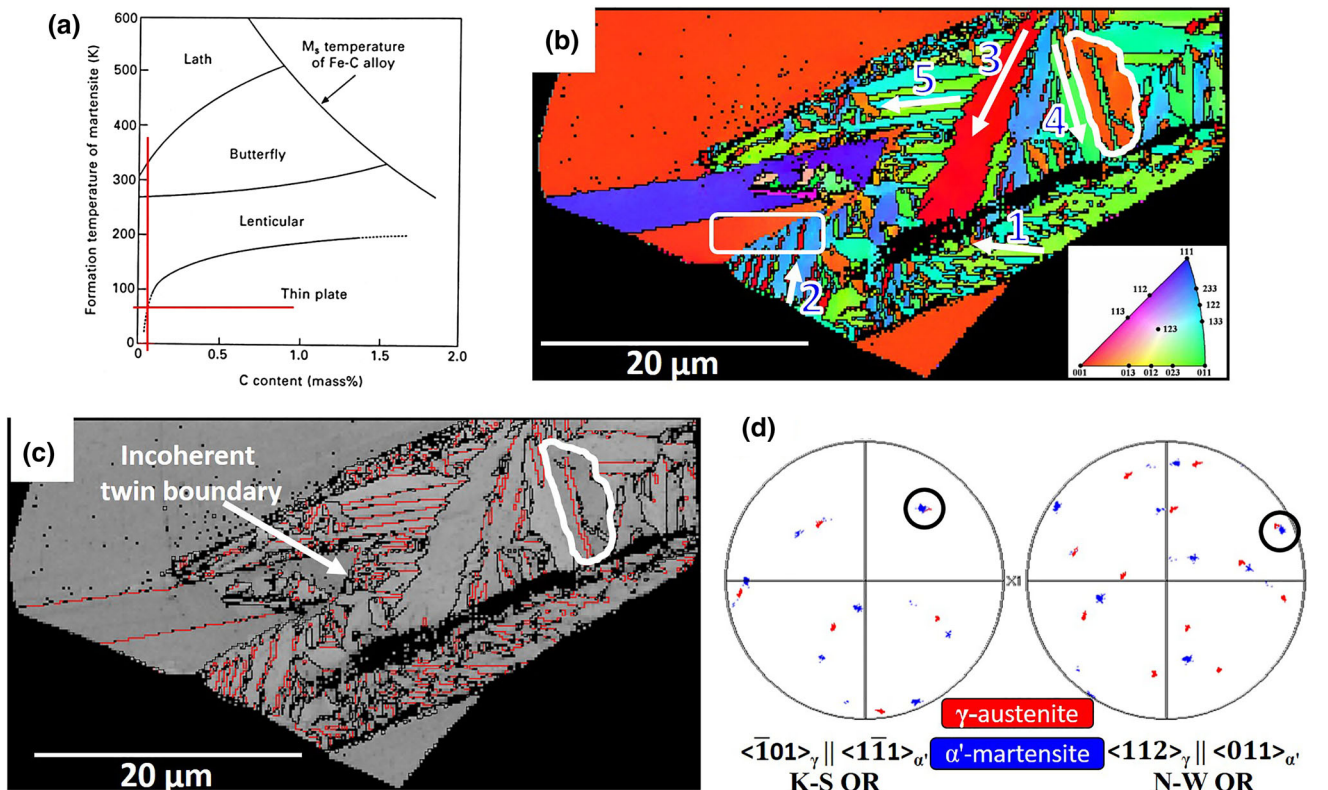


Fig. 10—(a) Schematic drawing showing the formation range of  $\alpha'$  as a function of  $M_s$  temperature and carbon concentration in Fe-Ni-C alloy systems, reprinted from Ref. [24], with permission; (b) phase and (c) BC/twin maps of  $RD||[100]$  oriented austenite grain in Fig. 8; (d) co-plot of  $\langle\bar{1}01\rangle_{\gamma}$  and  $\langle\bar{1}\bar{1}1\rangle_{\alpha'}$  and  $\langle112\rangle_{\gamma}$  and  $\langle011\rangle_{\alpha'}$  pole figures of marked rectangular region in (b).

are grouped together due to the absence of concurrent stabilization common to both.<sup>[28]</sup> This may justify their (bursting and isothermal behaviors) co-existence in Figure 10.

Although the EBSD results suggest the isothermally-induced martensite have thin-plate morphology, it has been reported that this morphology could become lenticular under certain conditions. On the effect of deformation temperature on the stress-induced growth behavior of thin-plate martensite, Shibata *et al.*<sup>[26]</sup> observed that thermally-transformed thin-plate  $\alpha'$  grows without a change in morphology when deformation is at a temperature close to the  $M_s$  temperature. A shape change into lenticular, however, occurs at a temperature above the  $M_s$  temperature, leading to the conclusion that midrib in lenticular  $\alpha'$  was thin-plate  $\alpha'$  at an earlier formation stage. During the isothermal holding of Fe-1.0C-17Cr (wt pct) stainless steel in liquid nitrogen ( $-196^{\circ}\text{C}$ ), Lee *et al.*<sup>[23]</sup> observed that thin-plate martensite first formed, followed by the lenticular martensite after an extended period. This observation is contrary to the general opinion that lenticular  $\alpha'$  forms at a higher temperature than the temperature at which thin-plate  $\alpha'$  evolves. It is, therefore, possible that the thermally-induced thin-plate  $\alpha'$  in AISI 321 steel will grow into lenticular  $\alpha'$  at an extended time. This is validated by the presence of a  $RD||[100]$  oriented lenticular  $\alpha'$  (lenticular white highlight in Figures 10(b) and (c)) with a branched midrib. On the existing

orientation relationship between the untransformed  $\gamma$  and thin-plate  $\alpha'$ , the coincidence of poles when  $\langle\bar{1}01\rangle_{\gamma}$  and  $\langle\bar{1}\bar{1}1\rangle_{\alpha'}$  pole figures, and  $\langle112\rangle_{\gamma}$  and  $\langle011\rangle_{\alpha'}$  pole figures were superimposed in Figure 10(d) confirmed the existence of both Kurdjumov-Sachs ( $\{\bar{1}11\}_{\gamma}||\{\bar{1}10\}_{\alpha'}$  and  $\langle\bar{1}01\rangle_{\gamma}||\langle\bar{1}\bar{1}1\rangle_{\alpha'}$ ) and Nishiyama-Wasserman ( $\{\bar{1}11\}_{\gamma}||\{\bar{1}10\}_{\alpha'}$  and  $\langle112\rangle_{\gamma}||\langle011\rangle_{\alpha'}$ ) orientation relationships, respectively.

### B. Mechanical Stability of Austenite (MSA)

To determine the MSA in AISI 321 austenitic stainless steel, UFG, FG, and CG specimens were deformed at different strain rate regimes *i.e.*, under quasi-static and dynamic compressive loading conditions.

#### 1. True stress-strain curves and hardness profile

Typical true stress-strain curves of specimens deformed under quasi-static and dynamic loading conditions are presented in Figures 11(a) and (b), respectively. The mechanical strength of the alloy increases with a decrease in grain size under both deformation conditions. However, specimens compressed under quasi-static condition strain hardens up to the final deformation strain while those specimens subjected to dynamic loading conditions show strain hardening that is eventually overcome by thermal softening. The

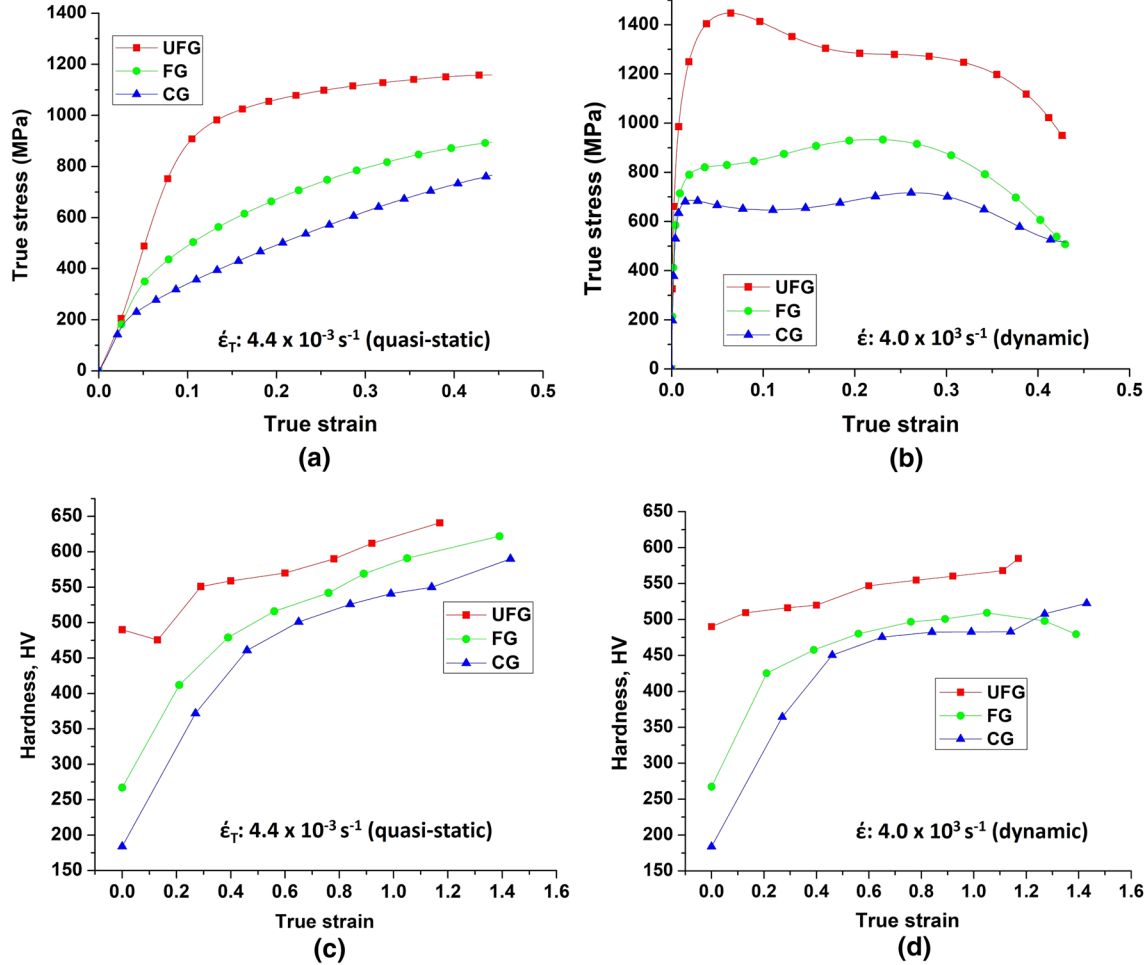


Fig. 11—(a) and (b) Typical true stress–strain and (c) and (d) hardness–true strain curves for specimens compressed under quasi-static and dynamic loading conditions.

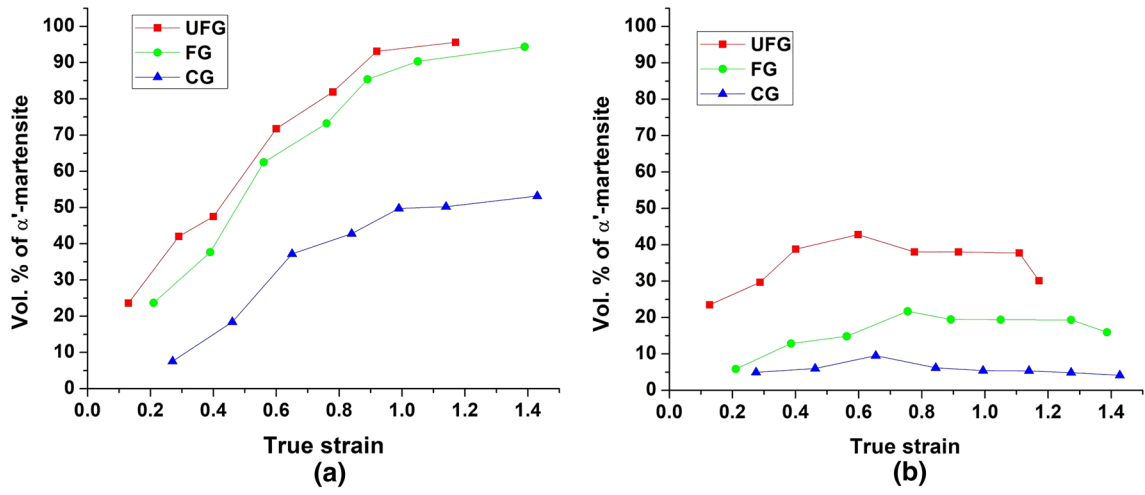


Fig. 12—Volume percent of  $\alpha'$ -true strain curves for specimens compressed under (a) quasi-static and (b) dynamic loading conditions.

thermal softening leads to drop in flow stress and results in eventual loss of load-carrying capacity. Similarly, the hardness profile of specimens deformed under quasi-static and dynamic loading conditions are presented in

Figures 11(c) and (d), respectively. Although the hardness value of the alloy increases with decrease in grain size and increase in strain under both deformation conditions, those deformed under quasi-static condition

possesses higher hardness values. Hardening in AISI 321 steel has been attributed to multiple strengthening sources such as the simultaneous occurrence of slip, twinning, and martensitic phase transformation.<sup>[29]</sup> Due to the scope of this work, subsequent sections are now focused on the evolution pattern of deformation-induced martensitic phase transformation in the investigated steel.

## 2. Microstructural evaluation and morphology of deformation-induced martensite

Figure 12 shows the volume fraction of deformation-induced  $\alpha'$  and its variation with grain size and

strain in both low and high strain rate regimes. While the fraction of  $\alpha'$  increases with strain (irrespective of grain size) in specimens deformed under the quasi-static loading condition (Figure 12(a)), those of the specimens subjected to dynamic loading condition increased with strain up to a critical value above which the fraction of  $\alpha'$  drops (Figure 12(b)). The drop in  $\alpha'$  (Figure 12(b)) is attributed to the temperature rise (adiabatic heating) in the impacted specimen, which is a signature of high strain rate loading condition.<sup>[30–33]</sup> On the stability of the austenite phase under external compressive load, Figure 12 shows that the mechanical stability of austenite in metastable AISI 321 austenitic stainless steel

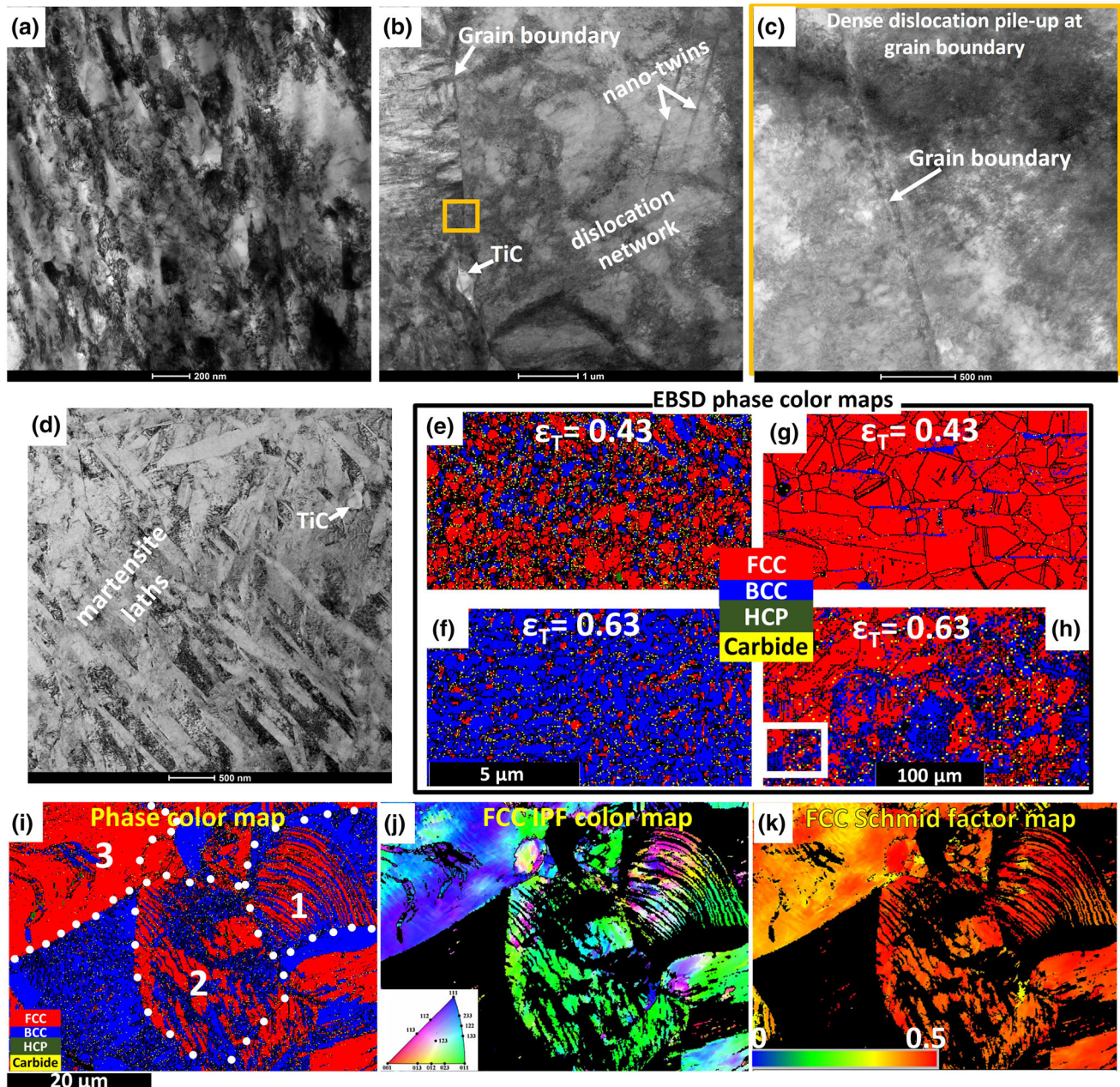


Fig. 13—(a) through (d) TEM micrographs: (a) UFG and (b) through (d) CG specimens; (e) through (h) EBSD phase maps: (e), (f) UFG and (g), (h) CG specimens compressed under quasi-static conditions; and ((i) through (k)) Higher magnification EBSD maps of marked region in (h): (i) phase color, (j) FCC IPF color, and (k) FCC Schmid factor maps.

decreases with a decrease in grain size since the fraction of deformation-induced  $\alpha'$  increases with a decrease in grain size. The reverse was observed to be the case for thermal stability of austenite (TSA) as discussed in the previous subsection.

The TEM micrographs of specimens compressed under the quasi-static condition (Figures 13(a) through (d)) shows the morphology of deformation-induced  $\alpha'$  that is distinctively different from that of the thermally-induced  $\alpha'$ . Unlike the  $\gamma$  in UFG specimens that are perfectly stable in cryogenic environment, the  $\gamma$  in UFG specimen are very unstable under an external compressive load and the morphology of deformation-induced  $\alpha'$  is equiaxed (Figure 13(a)). The TEM micrographs of the CG specimen subjected to quasi-static compressive load are presented in Figures 13(b) through (d). It can be confirmed in Figure 13(b) that high dislocation densities and nano-twins are present in the remaining austenite phase. Figure 13(d) shows that the morphology of deformation-induced  $\alpha'$  in CG specimens is lath-like, which are  $\sim 70$  nm thick and  $\sim 830$  nm long. The size of the laths could justify why  $\alpha'$  in UFG specimen retains the morphology of the  $\gamma$  (equiaxed); since  $\alpha'$  laths are  $\sim 3.5$  times longer than the  $\gamma$  grain size of UFG specimen. The evolution of lath-like  $\alpha'$  in compressed CG specimens rather than thin-plate  $\alpha'$ , as in the case of thermally-treated CG specimen, could be due to the different temperature regimes at which thermal ( $-196^{\circ}\text{C}$ ) and mechanical ( $23^{\circ}\text{C}$ ) tests were

conducted. It has been reported elsewhere<sup>[25]</sup> that the morphology of  $\alpha'$  can be influenced by temperature as also shown in Figure 10(a). Qualitatively, the EBSD phase maps in Figures 13(e) through (h) show the austenite phase in the UFG specimen to be more unstable than the CG specimen, and the instability increases with strain. This result agrees with the quantitative feritscope results in Figure 12(a). The formation of a higher fraction of  $\alpha'$  in UFG specimens is due to the higher grain boundary area and triple junctions that are nucleation sites for deformation-induced  $\alpha'$  transformation.<sup>[34,35]</sup>

On the role of texture on the mechanical stability of  $\gamma$ , the  $\gamma$  stability in AISI 321 increases from  $\text{CD}||[100]$  to  $\text{CD}||[110]$  and to  $\text{CD}||[111]$ , in that order, for FG and CG specimens. In this case, CD is the compression direction. This observation is also reported elsewhere.<sup>[36]</sup> This is affirmed by considering  $\gamma$  grains 1, 2, and 3 in the EBSD phase maps for a compressed CG specimen (Figure 13(i)), which are oriented near  $\text{CD}||[100]$ ,  $\text{CD}||[110]$ , and  $\text{CD}||[111]$ , respectively (Figure 13(j)). These grains underwent deformation-induced martensitic phase transformation with the highest mechanical instability of  $\gamma$  phase recorded in grain 1, followed by grains 2 and 3, in that order. Schmid factor map for the austenite phase (Figure 13(k)) shows that the most mechanically-stable of  $\gamma$ , grain 3, possesses the lowest Schmid factor, while  $\gamma$  grain 1 is the least stable with highest Schmid factor. The Schmid factor,

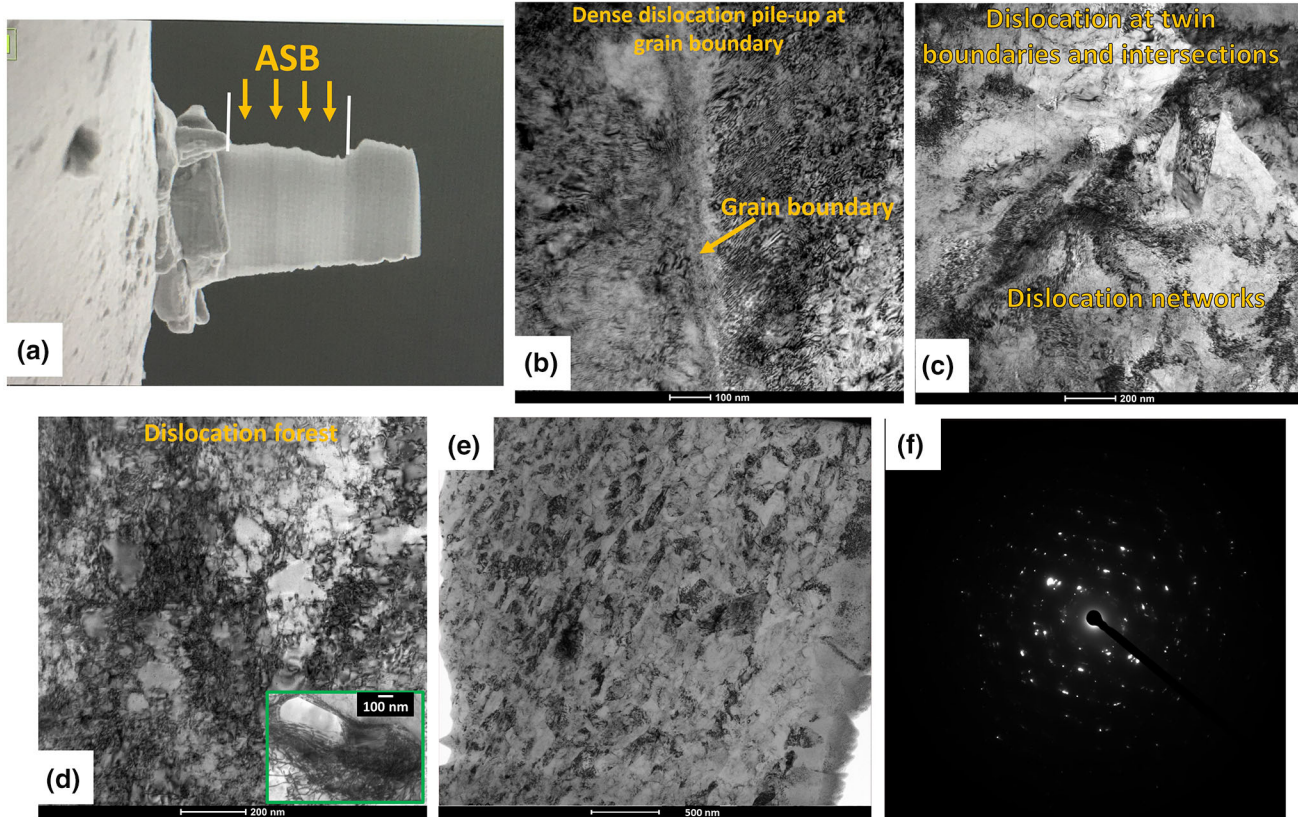


Fig. 14—TEM micrographs of dynamic-impacted specimens: (a) Fibbed specimen showing inside and outside regions of ASB, (b) through (d) outside ASB, (e) inside ASB, (f) selected area diffraction pattern for (e). Inset in (d) shows carbide-dislocations interaction.

therefore, suggests that grain 1 (grain oriented near  $CD \parallel [100]$ ) demonstrate ease of slip system activation compared to grains of other orientations during compression.<sup>[37–39]</sup>

TEM micrographs of CG specimen subjected to dynamic impact loading condition are presented in Figure 14. A narrow shear zone, termed adiabatic shear band (ASB), that eventually become preferential dynamic failure/fracture sites is typically observed in the microstructure of materials subjected to dynamic impact load.<sup>[40,41]</sup> In a CG specimen that forms ASB (Figure 14), the region outside the ASB shows grain boundary-dislocation interaction (Figure 14(b)), twin boundary-dislocation interaction (Figure 14(c)) and regions of dislocation forest in deformed austenite (Figure 14(c)). The TEM micrographs of the region inside ASB (Figures 14(e) and (f)) confirmed the occurrence of grain refinement which has been attributed to rotational dynamic recrystallization proposed by Nesterenko *et al.*<sup>[42]</sup> The EBSD phase maps of inside and outside ASB of impacted UFG (Figures 15(a) through (c)) and CG (Figures 15(d) and (e)) specimens show that inhomogeneous deformation results in inhomogeneous phase distribution, *i.e.*, the fraction of strain induced  $\alpha'$  transformation is highest outside ASB and very low inside the ASB. The near-absence of  $\alpha'$  in the ASB

region (Figures 15(c) and (e)) justifies that the temperature rise in these specimens are significantly high (to suppress phase transformation) and localized. Although the mechanical stability of the  $\gamma$  phase is higher in specimens deformed under dynamic condition (Figure 15) than those under quasi-static condition (Figure 13), it can also be confirmed from Figure 15 that the mechanical stability of the  $\gamma$  decreases with a decrease in grain size. On the morphology of deformation-induced  $\alpha'$  in specimens deformed under dynamic condition, the morphology of  $\alpha'$  in UFG specimen are equiaxed (Figure 15(b)) while those in CG specimen are irregular with no definite shape (Figure 15(d)). Based on the above experimental data and discussion of results, the role of grain size, texture, strain, and strain rate on the thermal and the mechanical stability of austenite in AISI 321 stainless steel can be summarized in a schematic diagram as shown in Figure 16.

#### IV. SUMMARY AND CONCLUSIONS

The roles of grain size, texture, strain, and strain rate on the thermal and mechanical stability of austenite in AISI 321 metastable austenitic stainless steel were studied. Ultrafine grain (UFG), fine grain (FG), and

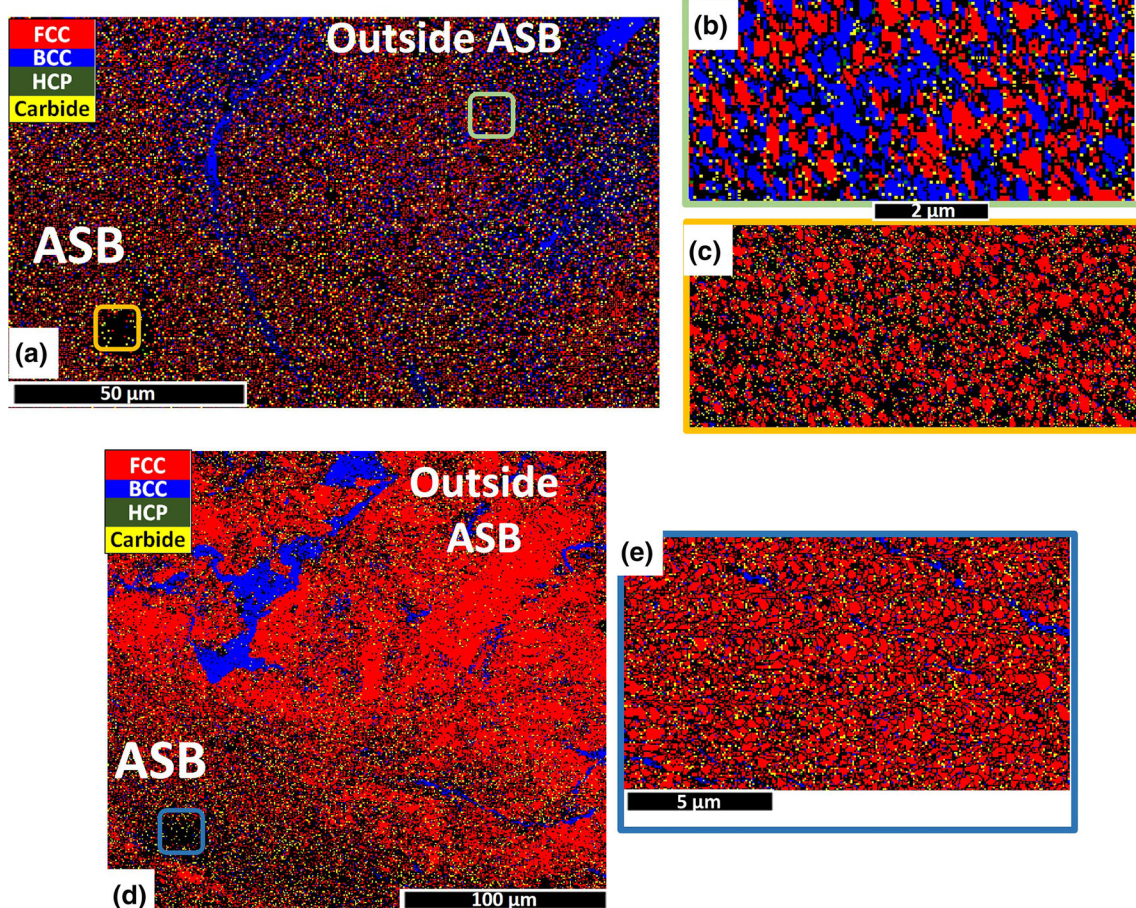


Fig. 15—EBSD phase maps of dynamic-impacted specimens showing inside and outside ASB regions: (a) to (c) UFG and (d), (e) CG specimens.

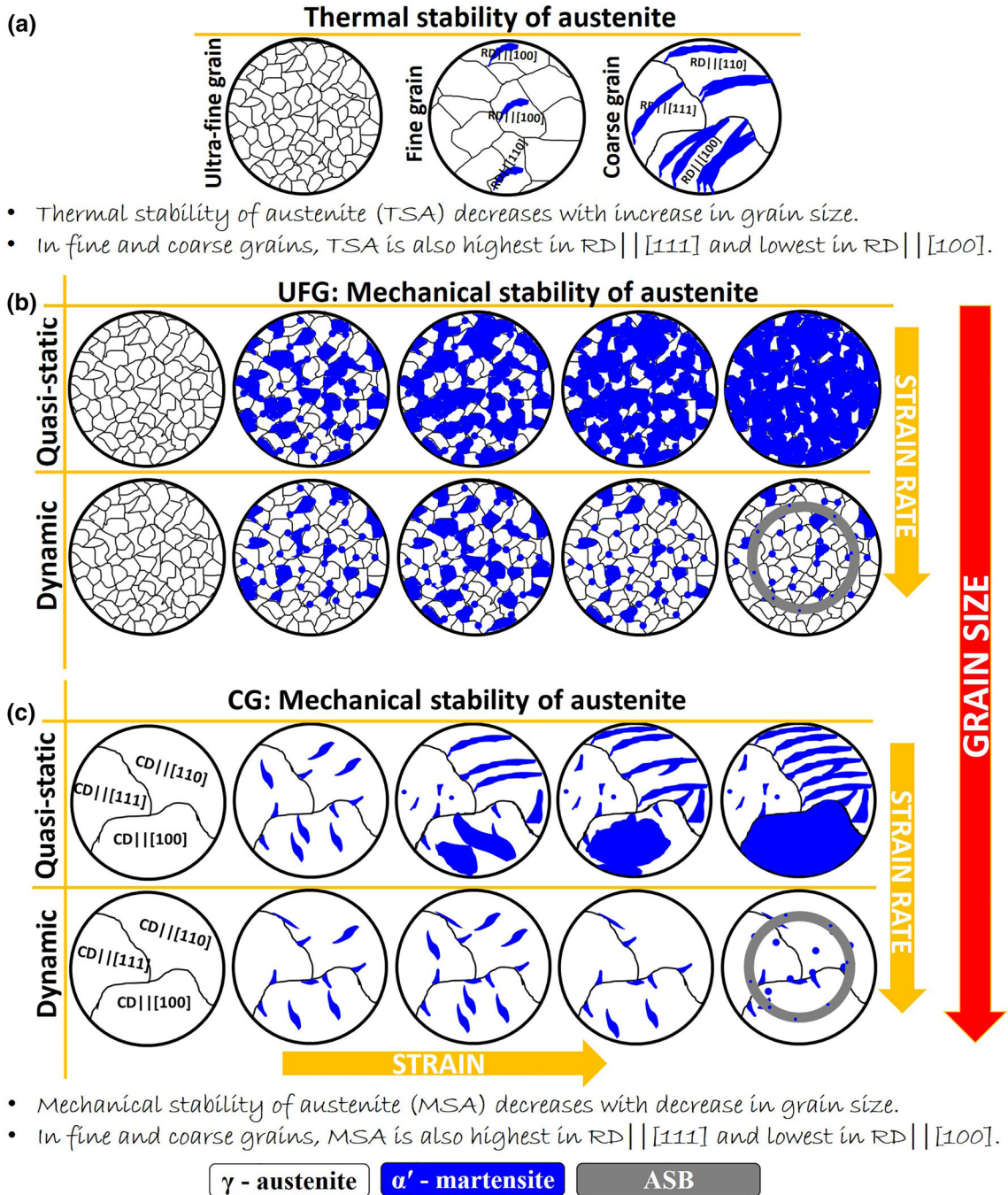


Fig. 16—Schematic drawing showing the role of grain size on (a) thermal and (b), (c) mechanical stability of austenite in AISI 321 stainless steel.

coarse grain (CG) specimens with average grain sizes of 0.24, 3, and 37  $\mu\text{m}$  sizes, respectively, were investigated. Samples were soaked in liquid nitrogen ( $-196^\circ\text{C}$ ) for 30 minutes, 1, 12, and 24 hours to determine the thermal stability of austenite (TSA). On the other hand, the mechanical stability of austenite (MSA) was studied by subjecting cylindrical specimens to both quasi-static ( $4.4 \times 10^{-3} \text{ s}^{-1}$ ) and dynamic loading conditions (between  $1300$  and  $8800 \text{ s}^{-1}$ ). The following conclusions are drawn from the research findings;

1. Thermally-induced  $\alpha'$ -martensite can only be observed at an incubant time in AISI 321, suggesting the occurrence of an isothermal martensitic transformation. Both Kurdjumov-Sachs ( $\{\{111\}_\gamma \parallel \{110\}_{\alpha'}$  and  $\langle 101 \rangle_\gamma \parallel \langle 111 \rangle_{\alpha'}$ ) and Nishiyama-Wasserman ( $\{\{111\}_\gamma \parallel \{110\}_{\alpha'}$  and  $\langle 112 \rangle_\gamma \parallel \langle 011 \rangle_{\alpha'}$ ) orientation relationships exist between the untransformed  $\gamma$  and thin-plate  $\alpha'$ . The phase transformation is highly suppressed in UFG specimens.

2. While TSA decreases with an increase in grain size, MSA decreases with a decrease in grain size.
3. The higher mechanical instability of austenite in UFG specimen under compression is due to the presence of higher grain boundary area and triple junctions that promote deformation-induced phase transformation. Meanwhile, the higher austenite stability of UFG specimen in cryogenic temperature is due to spatial restriction effect that resists the formation of isothermal martensite. This subsequently restricts multi-variant transformation required to accommodate anisotropic transformation strain.
4. While thin-plate  $\alpha'$  is predominantly formed in thermally-treated AISI 321 steel (FG and CG specimens only), lath and irregularly-shaped  $\alpha'$  are formed in specimens deformed under quasi-static and dynamic loading conditions, respectively. Irrespective of strain rate, deformation-induced  $\alpha'$  in UFG specimens inherit the equiaxed morphology of the deformed austenite grain.
5. Irrespective of grain size, MSA also decreases with an increase in strain and decrease in strain rate. In the event of ASB formation in specimens deformed at high strain rate, MSA increases as the ASB is approached. This is due to the significant temperature rise inside the ASB region.
6. EBSD analysis revealed that the evolution of both thermally- and deformation-induced martensite is orientation-dependent in FG and CG specimens. The instability (both thermal and mechanical) of the austenite phase was observed to be highest in the RD/CD|[100]-oriented grains, followed by grains oriented near RD/CD|[110] and RD/CD|[111], in that order. These findings could open a new window of engineering the initial texture of metastable austenitic stainless steel to either aid thermally or mechanically-stable austenite phase or promote both isothermal and deformation-induced martensitic phase transformation.
4. T. Kakeshita, T. Saburi, and K. Shimizu: *Philos. Mag. B Phys. Condens. Matter Stat. Mech. Electron. Opt. Magn. Prop.*, 2000, vol. 80, pp. 171–81.
5. E. Yasar, E. Güler, H. Güngünes, and T.N. Durlu: *Mater. Charact.*, 2008, vol. 59, pp. 769–72.
6. T. Kakeshita, K. Kuroiwa, K. Shimizu, T. Ikeda, A. Yamagishi, and M. Date: *Mater. Trans. JIM*, 1993, vol. 34, pp. 423–28.
7. D.E. Laughlin, N.J. Jones, A.J. Schwartz, and T.B. Massalski: *Int. Conf. Martensitic Transform.*, 2013, vol. 2008, pp. 141–44.
8. J.M. Nam, T. Terai, and T. Kakeshita: *J. Alloys Compd.*, 2013, vol. 577, pp. S348–52.
9. I.Y. Georgieva and I.I. Nikitina: *Met Sci Heat Treat*, 1972, vol. 5, pp. 68–72.
10. D.Z. Yang and C.M. Wayman: *Scr. Metall.*, 1983, vol. 17, pp. 1377–79.
11. M.B. Leban and R. Tisu: *Eng. Fail. Anal.*, 2013, vol. 33, pp. 430–38.
12. K. Spencer, J.D. Embury, K.T. Conlon, M. Véron, and Y. Bréchet: *Mater. Sci. Eng. A*, 2004, vols. 387–389, pp. 873–81.
13. P.R. Rios, G. da Silva Drumond, T. Neves, and J.R.C. Guimarães: *Mater. Sci. Forum*, 2014, vols. 783–786, pp. 2182–87.
14. A.A. Tiamiyu, J.A. Szpunar, A.G. Odeshi, I. Oguocha, and M. Eskandari: *Metall. Mater. Trans. A*, 2017, vol. 48A, pp. 5990–6012.
15. C. Weinong and S. Bo: *Split Hopkinson (Kolsky) Bar: Design, Testing and Applications (Mechanical Engineering Series)*, Illustrate, Springer Science & Business Media, New York, 2010.
16. J. Talonen, P. Aspereen, and H. Hänninen: *Mater. Sci. Technol.*, 2004, vol. 20, pp. 1506–12.
17. Y.F. Shen, N. Jia, Y.D. Wang, X. Sun, L. Zuo, and D. Raabe: *Acta Mater.*, 2015, vol. 97, pp. 305–15.
18. H.F.G. De Abreu, S.S. De Carvalho, P. De Lima Neto, R.P. Dos Santos, V.N. Freire, P.M.D.O. Silva, and S.S.M. Tavares: *Mater. Res.*, 2007, vol. 10, pp. 359–66.
19. H.K.D.H. Bhadeshia and R.W.K. Honeycombe: in *Steels: Microstructure and Properties*, Third edition, Butterworth-Heinemann, Boston, 2006, pp. 95–128.
20. Y. Matsuoka, T. Iwasaki, N. Nakada, and T. Tsuchiyama: *ISIJ Int.*, 2013, vol. 53, pp. 1224–30.
21. Y.L. Chang, P.Y. Chen, Y.T. Tsai, and J.R. Yang: *Mater. Charact.*, 2016, vol. 113, pp. 17–25.
22. L. Bracke, K. Verbeken, L. Kestens, and J. Penning: *Acta Mater.*, 2009, vol. 57, pp. 1512–24.
23. H.Y. Lee, H.W. Yen, H.T. Chang, and J.R. Yang: *Scr. Mater.*, 2010, vol. 62, pp. 670–73.
24. T. Maki: in *Phase Transformations in Steels*, Woodhead Publishing, Oxford, 2012, pp. 34–58.
25. M. Umehoto, E. Yoshitake, and I. Tamura: *J. Mater. Sci.*, 1983, vol. 18, pp. 2893–904.
26. A. Shibata, T. Murakami, S. Morito, T. Furuhara, and T. Maki: *Mater. Trans.*, 2008, vol. 49, pp. 1242–48.
27. S. Kajiwara and W.S. Owen: *Scr. Metall.*, 1977, vol. 11, pp. 137–42.
28. N.N. Thadhani and M.A. Meyers: *Prog. Mater. Sci.*, 1986, vol. 30, pp. 1–37.
29. A.A. Tiamiyu, A.G. Odeshi, and J.A. Szpunar: *Mater. Sci. Eng. A*, 2018, vol. 711, pp. 233–49.
30. A. Kundu and P.C. Chakraborti: *J. Mater. Sci.*, 2010, vol. 45, pp. 5482–89.
31. J.A. Lichtenfeld, M.C. Mataya, and C.J. Van Tyne: *Metall. Mater. Trans. A*, 2006, vol. 37A, pp. 147–61.
32. T. Iwamoto, T. Sawa, and M. Cherkaoui: *Int. J. Mod. Phys. B*, 2008, vol. 22, pp. 5985–90.
33. J. Talonen, H. Hänninen, P. Nenonen, and G. Pape: *Metall. Mater. Trans. A*, 2005, vol. 36A, pp. 421–32.
34. A. Das and S. Tarafder: *Int. J. Plast.*, 2009, vol. 25, pp. 2222–47.
35. H. Yen, S.W. Ooi, M. Eizadjou, A. Breen, C. Huang, H.K.D.H. Bhadeshia, and S.P. Ringer: *Acta Mater.*, 2015, vol. 82, pp. 100–14.
36. A.A. Tiamiyu, V. Tari, J.A. Szpunar, A.G. Odeshi, and A.K. Khan: *Int. J. Plast.*, 2018, vol. 107, pp. 79–99.

## ACKNOWLEDGMENTS

Authors wish to acknowledge the financial support of Natural Sciences and Engineering Research Council of Canada (NSERC). A.A. Tiamiyu acknowledges the financial support provided by the Vanier Canada Graduate Scholarship for this study. The support of ACUREN Group Inc. for the use of Fischer Fertscope MP30E is well appreciated.

## REFERENCES

1. J.Y. Choi, T. Fukuda, and T. Kakeshita: *Mater. Sci. Forum*, 2010, vols. 654–656, pp. 130–33.
2. P.R. Rios and J.R.C. Guimarães: *Mater. Res.*, 2016, vol. 19, pp. 490–95.
3. H. Zheng, W. Wang, D. Wu, S. Xue, Q. Zhai, J. Frenzel, and Z. Luo: *Intermetallics*, 2013, vol. 36, pp. 90–95.

4. T. Kakeshita, T. Saburi, and K. Shimizu: *Philos. Mag. B Phys. Condens. Matter Stat. Mech. Electron. Opt. Magn. Prop.*, 2000, vol. 80, pp. 171–81.
5. E. Yasar, E. Güler, H. Güngünes, and T.N. Durlu: *Mater. Charact.*, 2008, vol. 59, pp. 769–72.
6. T. Kakeshita, K. Kuroiwa, K. Shimizu, T. Ikeda, A. Yamagishi, and M. Date: *Mater. Trans. JIM*, 1993, vol. 34, pp. 423–28.
7. D.E. Laughlin, N.J. Jones, A.J. Schwartz, and T.B. Massalski: *Int. Conf. Martensitic Transform.*, 2013, vol. 2008, pp. 141–44.
8. J.M. Nam, T. Terai, and T. Kakeshita: *J. Alloys Compd.*, 2013, vol. 577, pp. S348–52.
9. I.Y. Georgieva and I.I. Nikitina: *Met Sci Heat Treat*, 1972, vol. 5, pp. 68–72.
10. D.Z. Yang and C.M. Wayman: *Scr. Metall.*, 1983, vol. 17, pp. 1377–79.
11. M.B. Leban and R. Tisu: *Eng. Fail. Anal.*, 2013, vol. 33, pp. 430–38.
12. K. Spencer, J.D. Embury, K.T. Conlon, M. Véron, and Y. Bréchet: *Mater. Sci. Eng. A*, 2004, vols. 387–389, pp. 873–81.
13. P.R. Rios, G. da Silva Drumond, T. Neves, and J.R.C. Guimarães: *Mater. Sci. Forum*, 2014, vols. 783–786, pp. 2182–87.
14. A.A. Tiamiyu, J.A. Szpunar, A.G. Odeshi, I. Oguocha, and M. Eskandari: *Metall. Mater. Trans. A*, 2017, vol. 48A, pp. 5990–6012.
15. C. Weinong and S. Bo: *Split Hopkinson (Kolsky) Bar: Design, Testing and Applications (Mechanical Engineering Series)*, Illustrate, Springer Science & Business Media, New York, 2010.
16. J. Talonen, P. Aspereen, and H. Hänninen: *Mater. Sci. Technol.*, 2004, vol. 20, pp. 1506–12.
17. Y.F. Shen, N. Jia, Y.D. Wang, X. Sun, L. Zuo, and D. Raabe: *Acta Mater.*, 2015, vol. 97, pp. 305–15.
18. H.F.G. De Abreu, S.S. De Carvalho, P. De Lima Neto, R.P. Dos Santos, V.N. Freire, P.M.D.O. Silva, and S.S.M. Tavares: *Mater. Res.*, 2007, vol. 10, pp. 359–66.
19. H.K.D.H. Bhadeshia and R.W.K. Honeycombe: in *Steels: Microstructure and Properties*, Third edition, Butterworth-Heinemann, Boston, 2006, pp. 95–128.
20. Y. Matsuoka, T. Iwasaki, N. Nakada, and T. Tsuchiyama: *ISIJ Int.*, 2013, vol. 53, pp. 1224–30.
21. Y.L. Chang, P.Y. Chen, Y.T. Tsai, and J.R. Yang: *Mater. Charact.*, 2016, vol. 113, pp. 17–25.
22. L. Bracke, K. Verbeken, L. Kestens, and J. Penning: *Acta Mater.*, 2009, vol. 57, pp. 1512–24.
23. H.Y. Lee, H.W. Yen, H.T. Chang, and J.R. Yang: *Scr. Mater.*, 2010, vol. 62, pp. 670–73.
24. T. Maki: in *Phase Transformations in Steels*, Woodhead Publishing, Oxford, 2012, pp. 34–58.
25. M. Umehoto, E. Yoshitake, and I. Tamura: *J. Mater. Sci.*, 1983, vol. 18, pp. 2893–904.
26. A. Shibata, T. Murakami, S. Morito, T. Furuhara, and T. Maki: *Mater. Trans.*, 2008, vol. 49, pp. 1242–48.
27. S. Kajiwara and W.S. Owen: *Scr. Metall.*, 1977, vol. 11, pp. 137–42.
28. N.N. Thadhani and M.A. Meyers: *Prog. Mater. Sci.*, 1986, vol. 30, pp. 1–37.
29. A.A. Tiamiyu, A.G. Odeshi, and J.A. Szpunar: *Mater. Sci. Eng. A*, 2018, vol. 711, pp. 233–49.
30. A. Kundu and P.C. Chakraborti: *J. Mater. Sci.*, 2010, vol. 45, pp. 5482–89.
31. J.A. Lichtenfeld, M.C. Mataya, and C.J. Van Tyne: *Metall. Mater. Trans. A*, 2006, vol. 37A, pp. 147–61.
32. T. Iwamoto, T. Sawa, and M. Cherkaoui: *Int. J. Mod. Phys. B*, 2008, vol. 22, pp. 5985–90.
33. J. Talonen, H. Hänninen, P. Nenonen, and G. Pape: *Metall. Mater. Trans. A*, 2005, vol. 36A, pp. 421–32.
34. A. Das and S. Tarafder: *Int. J. Plast.*, 2009, vol. 25, pp. 2222–47.
35. H. Yen, S.W. Ooi, M. Eizadjou, A. Breen, C. Huang, H.K.D.H. Bhadeshia, and S.P. Ringer: *Acta Mater.*, 2015, vol. 82, pp. 100–14.
36. A.A. Tiamiyu, V. Tari, J.A. Szpunar, A.G. Odeshi, and A.K. Khan: *Int. J. Plast.*, 2018, vol. 107, pp. 79–99.

37. W.S. Choi, S. Sandlöbes, N.V. Malyar, C. Kirchlechner, S. Korte-Kerzel, G. Dehm, B.C. De Cooman, and D. Raabe: *Acta Mater.*, 2017, vol. 132, pp. 162–73.
38. L. Wang, J.C. E, Y. Cai, F. Zhao, D. Fan, and S.N. Luo: *J. Appl. Phys.*, 2015, vol. 117, p. 084301.
39. M. Karlsen, Ø. Grong, M. Søfferud, J. Hjelen, G. Rørvik, and R. Chiron: *Metall. Mater. Trans. A*, 2009, vol. 40, pp. 310–20.
40. H. Zhan, W. Zeng, G. Wang, D. Kent, and M. Dargusch: *Mater. Charact.*, 2015, vol. 102, pp. 103–13.
41. J. Peirs, W. Tirry, B. Amin-Ahmadi, F. Coghe, P. Verleysen, L. Rabet, D. Schryvers, and J. Degrieck: *Mater. Charact.*, 2013, vol. 75, pp. 79–92.
42. V.F. Nesterenko, M.A. Meyers, J.C. LaSalvia, M.P. Bondar, Y.J. Chen, and Y.L. Lukyanov: *Mater. Sci. Eng. A*, 1997, vol. 229, pp. 23–41.

**Publisher's Note** Springer Nature remains neutral with regard to jurisdictional claims in published maps and institutional affiliations.